

1 **An inverse method to derive surface fluxes from the closure**
2 **of oceanic heat and water budgets:**
3 **application to the north-western Mediterranean Sea**
4

5 **G. Caniaux¹, L. Prieur², H. Giordani¹, and J.-L. Redelsperger³**

6 ¹CNRM-UMR3589 (Météo-France/CNRS), Toulouse, France

7 ²Sorbonne Universités, UPMC Univ. Paris 06, INSU-CNRS-UMR7093, Laboratoire
8 d'Océanographie de Villefranche (LOV), Villefranche-sur-Mer, France

9 ³UBO/CNRS-UMR6523, Brest, France

10
11 Corresponding author: Guy Caniaux (guy.caniaux@meteo.fr)

12 Louis Prieur (prieur@obs-vlfr.fr)

13 Hervé Giordani (herve.giordani@meteo.fr)

14 Jean-Luc Redelsperger (jean.luc.redelsperger@ifremer.fr)

15
16 **Key Points:**

- 17 • Hourly surface fluxes are produced with an inverse method over the north-western
18 Mediterranean, during one year at a fine spatial scale
- 19 • With the fluxes deduced from the inverse method, the annual heat and water budgets
20 are closed within some $W m^{-2}$ and some $mm yr^{-1}$
- 21 • Compared with the adjusted fluxes, numerical prediction models are evaluated : they
22 fail to retrieve the mean annual patterns and values
23

23 **Abstract**

24 The large amount of data collected during DeWEX, MOOSE and HyMeX campaigns in the
25 north-western Mediterranean in 2012-2013 allowed to implement an inverse method to solve the
26 difficult problem of heat and water budget closure. The inverse method is based on the
27 simulation of the observed heat and water budgets, strongly constrained by observations
28 collected during the campaigns and on the deduction of adjusted surface fluxes. The inverse
29 method uses a genetic algorithm that generates 50.000 simulations of a single-column model and
30 optimizes some adjustable coefficients introduced in the surface fluxes. Finally, the single-
31 column model forced by the adjusted fluxes during one year and over a test area of about 300 x
32 300 km² simulates the daily mean satellite SST with an accuracy of 0.011°C, as well as daily
33 mean SSS and residual buoyancy series deduced from wintertime analyses with an accuracy of
34 0.011 and 0.03 m² s⁻² respectively. The adjusted fluxes close the annual heat and rescaled water
35 budgets by less than 5 W m⁻². To our knowledge, this is the first time that such a flux dataset is
36 produced. It can thus be considered as a reference for the north-western Mediterranean and be
37 used for estimating other flux datasets, for forcing regional models and for process studies.
38 Compared with the adjusted fluxes, some operational numerical weather prediction models
39 (ARPEGE, NCEP, ERA-INTERIM, ECMWF and AROME), often used to force oceanic models,
40 were evaluated: they are unable to retrieve the mean annual patterns and values.

41 **Keywords**

42 Heat and water surface fluxes, Budget closure, North-western Mediterranean Sea, Air-sea
43 interactions, Inverse method

44 **Short title**

45 An inverse method for oceanic surface fluxes

46

46 **1. Introduction**

47 The knowledge of surface fluxes exchanged between the ocean and the atmosphere has
48 important issues: forcing oceanic models, studying the processes by which the ocean and the
49 atmosphere exchange energy and mass, getting climatological estimates of the variability of
50 ocean surface forcings, and evaluating their role in the Earth's climate system. In the last twenty
51 years, lots of gridded air-sea flux fields, derived from in-situ observation analyses, from
52 numerical model reanalyses, from satellite retrievals or from merging satellite and numerical
53 model outputs were produced [e.g., *Large and Yeager, 2009; Valdivieso et al., 2015; Jordà et*
54 *al., 2016* for the Mediterranean]. However, surface flux fields are difficult to estimate because
55 they are highly dependent (1) of the biases which affect empirical bulk formulae, (2) of
56 uncertainties in exchange coefficients (especially at low and high winds), (3) of imperfect
57 boundary layer parameterizations (see the review by *Cronin et al., 2014*), and (4) of the spatial
58 and temporal resolutions of flux-related variables [*Artale et al., 2002; Ruti et al., 2008*]. In
59 consequence, few flux datasets are able to close budgets for the global ocean [*Valdivieso et al.,*
60 *2015*] or at basin-scale [*Castellari et al., 1998; Sanchez-Gomez et al., 2011*]. Urgent
61 improvements are also needed for radiative [*Liu et al., 2015*] and water budgets [*Bowman et al.,*
62 *2009; Romanou et al., 2010* for the Mediterranean].

63 Moreover, errors and uncertainties affecting fluxes lead forced oceanic models or coupled
64 models to diverge [*Rosati and Miyakoda, 1988*]. Generally modelers use restoring terms in the
65 scalar equations to prevent the model solution to drift from prescribed values or from the mean
66 climatological state [*Barnier et al., 1995*]. However, relaxation techniques alter and modify the
67 model thermodynamics and may produce distortions in annual cycles [*Killworth et al., 2000*],
68 and over longer time scales, may alter or even suppress some internal modes of variability
69 [*Simmons and Poyakov, 2004*]. Another expedient consists in correcting surface fluxes [*Large*
70 *and Yeager, 2009; Pettenuzzo et al., 2010*]. For that, many techniques have been used in different
71 regions of the world ocean in order to close heat and water budgets or at least to be consistent
72 with some constraints [see the review by *Large and Yeager, 2009*]. Some include inverse
73 methods by imposing oceanic constraints, like observed transports [*Isemer et al., 1989;*
74 *MacDonald and Wunsch, 1996*], and mixed layer heat contents [*Gaspar et al., 1990b*] or
75 atmospheric constraints, i.e., mass, moisture and energy budgets [*Trenberth, 1997*], temperature

76 Q1 and humidity Q2 budgets [Curry *et al.*, 1999]. Other studies propose linear inverse analyses
77 by using heat flux constraints [Grist and Josey, 2003], or assimilation of observations in
78 numerical models with the adjoint equation formalism of a one-dimensional [Roquet *et al.*, 1993]
79 or three-dimensional modeling approach [Stammer *et al.*, 2004; Yuan and Rienecker, 2003].
80 Variational objective analyses are another alternative to obtain best estimates of meteorological
81 variables needed to estimates surface fluxes [e.g., Yu *et al.*, 2004; Yu and Weller, 2007].

82 Caniaux *et al.* [2005b] tested an inverse method based on the optimization of numerous model
83 runs by a genetic algorithm to produce adjusted fluxes at a rather fine scale, in order to study
84 subduction in the north-eastern Atlantic. They showed that, if the region of study was well
85 sampled during a relatively long period of time (the POMME experiment in 2000-2001, Mémerly
86 *et al.*, 2005), the inverse method was particularly suitable to produce surface fluxes and to
87 simulate realistically the oceanic upper layers without any correction or restoring term [Paci *et*
88 *al.*, 2005; Giordani *et al.*, 2005] and to deduce reliable seasonal and annual subduction rates
89 [Paci *et al.*, 2007]. Here, we address the same question in a different context and region, i.e., in
90 the north-western Mediterranean (NWM).

91 The NWM is much more energetic than the intergyre region of the north-eastern Atlantic. The
92 basin is characterized by the presence of the Northern Mediterranean Current (or Liguro-
93 Provençal Current), which flows southwestward along the continental margin [Millot, 1987], and
94 further south by the northeastward return flow marked by the eddying Balearic front around
95 40°N [Send *et al.*, 1999; Poulain *et al.*, 2012]. The NWM is also known to form dense waters,
96 the Western Mediterranean Deep Waters (WMDW), during deep convective events [Rhein,
97 1995; Marshall and Schott, 1999]. Another difference is that surface fluxes are dominated by
98 frequent continental gale force winds [Bourassa *et al.*, 2013], associated with cold and dry air
99 masses that contrast significantly with the SSTs to generate important heat loss [Leaman and
100 Schott, 1991], i.e., in conditions where the errors and uncertainties which affect the bulk
101 formulae are the largest. Moreover, fine temporal and spatial resolution fluxes are crucial for
102 simulating correctly both the intensity and timing of intense mixing and deep oceanic
103 convection, given the low Rossby radius reached in winter and the stochastic nature of the
104 mechanisms at play [Castellari *et al.*, 2000; Herrmann and Somot, 2008; Béranger *et al.*, 2010].
105 There is also a clear need of accurate surface fluxes at fine temporal and spatial scales to produce

106 realistic estimates of dense water formation rates in the NWM [*Durrieu de Madron et al.*, 2013;
107 *Waldman et al.*, 2016].

108 As the NWM was extensively sampled from summer 2012 to summer 2013, with still more
109 numerous in-situ data than during the POMME campaigns, mostly due to gliders (nonexistent in
110 2000-2001) and to an increased number of ARGO floats, an attempt to test *Caniaux et al.*
111 [2005b]'s inverse method is exposed in the present paper. During one annual cycle, the NWM
112 was investigated in the frame of three scientific programs: the Mediterranean Ocean Observing
113 System for the Environment (MOOSE) [*Testor et al.*, 2012, 2013a], the Mediterranean Pelagic
114 Ecosystems Experiment (DeWEX) [*Testor*, 2013b; *Conan*, 2013] and the Hydrological Cycle of
115 the Mediterranean Experiment (HyMeX) [*Drobinski et al.*, 2014].

116 The paper is organized as follows: section 2 provides a description of the inverse method and
117 single-column model (SCM) approach. Results including the optimized corrections and
118 simulations are presented in section 3. In section 4, a local evaluation of the adjusted fluxes
119 against in-situ data, an evaluation of some numerical weather prediction models (NWPM) fields
120 and an estimate of the heat and water budget closure are provided. Conclusions are drawn in
121 section 5. Note that the SCM presented in section (2) can be used not only to optimize surface
122 forcings but also to study the physics of the near surface layers; for instance to investigate the
123 different processes at play in the evolution of SSTs, SSSs, of temperature and salinity profiles,
124 stratification and so on. A brief outline of this use of the SCM can be found in subsection 3.2 or
125 in *Caniaux et al.* [2015].

126 **2. Methodology**

127 **2.1. The Inverse Method**

128 The purpose of the inverse method is to perform many sensitivity tests with a numerical tool
129 forced at the surface with different sets of heat, water and momentum fluxes and to select the
130 best fluxes that allow to simulate realistically the evolution of a water column. For obvious
131 computer time reasons, it is impossible to use a three-dimensional (3D) model but rather a
132 simplified model, i.e., a SCM specially adapted to simulate a given area of the NWM (hereafter
133 the test area). From an initial estimate of the surface fluxes (hereafter the guess fluxes), and by
134 varying some adjustment coefficients for correcting the fluxes, an optimal set of these

135 coefficients is derived from the minimization of the distance between observed and modeled
 136 quantities (SSTs, SSSs, residual buoyancies, temperature and salinity profiles). We therefore
 137 impose a very strong constraint on the modeled evolution of the heat and water budgets, which
 138 results from the balance between lateral advective forces and surface fluxes. The choice of the
 139 best set of adjusted coefficients is done through the use of a genetic algorithm, an effective
 140 statistical tool for finding the minimum of particularly complex functions. Finally, thanks to the
 141 optimized coefficients, the guess fluxes can be corrected at any time step and any grid point of
 142 the test area, or of a somewhat larger surface area.

143 The SCM used is derived from the one-dimensional (1D) numerical model of vertical mixing
 144 developed by *Gaspar et al.* [1990a] and updated *Wade et al.* [2011]. It solves the heat, salt and
 145 momentum equations and is closed by a 1.5 turbulent scheme solving a turbulent kinetic energy
 146 equation. It includes a parameterization of the diapycnal mixing [*Large et al.*, 1994; *Kantha and*
 147 *Clayson*, 1994] to better represent non local sources of vertical mixing under the mixed layer
 148 depth. For the present study, the model was modified to take into account advection terms
 149 considered as external forcings, and added at each time step in the temperature and salinity
 150 equations. The model includes 450 regularly spaced levels of five meters and solves vertical
 151 turbulent mixing with a semi-implicit numerical scheme and a time step of one hour.

152 **2.2. Equations Solved**

153 The problem is to solve a set of equations fitted to describe an extended area, i.e., the equations
 154 of the temperature and salinity averaged over the test area itself, as well as their subgrid scale
 155 fluctuations. We start from the 3D temperature (or salinity) equation:

$$156 \quad \partial_t T = \frac{F_{sol} \partial_z I}{\rho_0 C_p} - \bar{u} \cdot \bar{\nabla}_h T - w \partial_z T - \partial_z (\overline{T'w'}) - \nabla_h \cdot (\overline{T'\bar{u}'}) \quad (1)$$

157 where the temperature tendency results from net solar radiation input F_{sol} , horizontal and vertical
 158 advections, vertical turbulent mixing (with the non-solar heat flux specified at the surface
 159 boundary, i.e., the sum of latent, sensible and net infra-red heat fluxes) and horizontal diffusion
 160 respectively. In equation (1), the single primes refer to the unresolved turbulent scales involved;
 161 $\partial_z I$ is the fraction of F_{sol} that penetrates at depth z ; ρ_0 and C_p are a reference surface density and

162 the specific heat capacity of sea water respectively. The horizontal and vertical advection terms
 163 $-\vec{u}\cdot\vec{\nabla}_h T$ and $-w\partial_z T$ were partitioned into Ekman (the horizontal Ekman current is denoted \vec{u}_e
 164 and the vertical Ekman velocity w_e) and non-Ekman components (\vec{u}_{ne} and w_{ne} respectively) so
 165 that (1) is rewritten as:

$$166 \quad \partial_t T = \frac{F_{sol}\partial_z I}{\rho_0 C_p} - \vec{u}_e \cdot \vec{\nabla}_h T - \vec{u}_{ne} \cdot \vec{\nabla}_h T - w_e \partial_z T - w_{ne} \partial_z T + \partial_z (K \partial_z T) - \nabla_h \cdot (\overline{T' \vec{u}'}) \quad (2)$$

167 in which the vertical turbulent fluxes ($-\overline{w'T'}$) in equation (1) were parameterized using the
 168 classical concept of eddy diffusivity ($K\partial_z T$). In *Caniaux et al.* [2005b], the horizontal and
 169 vertical non-Ekman advection terms were altogether derived from the evolution of mean
 170 temperature and salinity profiles deduced from four hydrological surveys performed during the
 171 one year of the POMME experiment. This hypothesis was valid as long as advection was a weak
 172 term in comparison with the other processes, not only near the surface but also at depth. This
 173 technique could not be used any more, since horizontal advection is highly depth dependent in
 174 the NWM and plays a much more important role in the top layers than at deeper levels (see
 175 subsections 2.4.3 and 3.2). This led us to hypothesize that the horizontal non-Ekman advection
 176 term could be represented by geostrophic advection, a term that could easily be deduced from the
 177 outputs of a 3D model run (see subsection 2.4.3).

178 As some non-linear terms in equation (2) can not be explicitly calculated at any point of the test
 179 area, they were split into spatial mean and deviation from this mean; this is the case for solar
 180 radiation, vertical Ekman advection and turbulent vertical mixing (respectively the 1st, 4th and 6th
 181 terms on the right hand side of equation (2)). After decomposing these terms into their spatial
 182 mean (angle brackets) and deviation (double prime) and after averaging each term over the test
 183 area (again with angle brackets), equation (2) becomes:

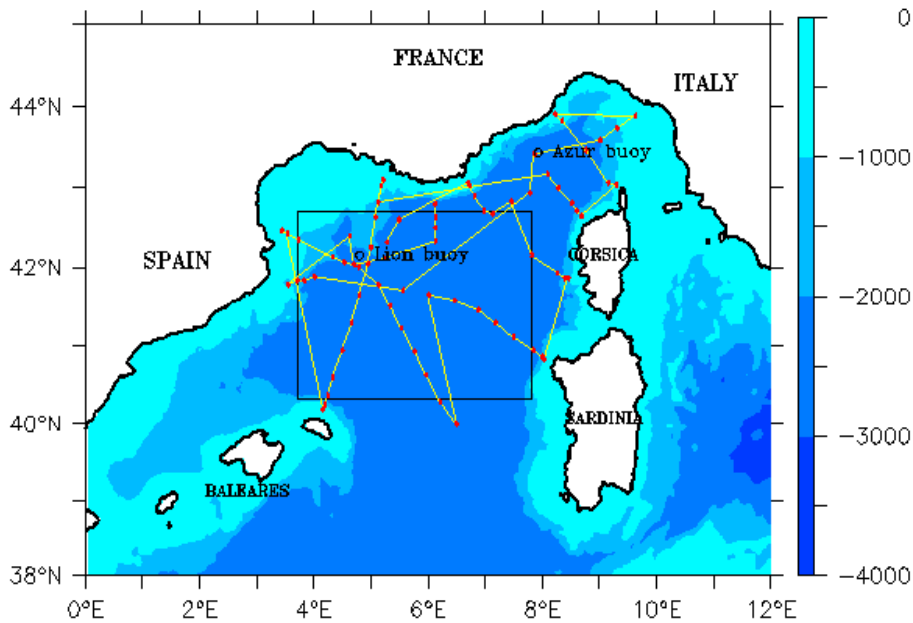
$$184 \quad \begin{aligned} \langle \partial_t T \rangle &= \frac{\langle F_{sol} \rangle \partial_z \langle I \rangle}{\rho_0 C_p} + \frac{\langle F_{sol}'' \partial_z I'' \rangle}{\rho_0 C_p} - \langle \vec{u}_e \cdot \vec{\nabla}_h T \rangle - \langle \vec{u}_{ne} \cdot \vec{\nabla}_h T \rangle \\ &- \langle w_e \partial_z T \rangle - \langle w_e'' \partial_z T'' \rangle - \langle w_{ne} \partial_z T \rangle \\ &+ \partial_z \langle K \rangle \partial_z \langle T \rangle + \partial_z \langle K'' \partial_z T'' \rangle - \langle \nabla_h \cdot (\overline{T' \vec{u}'}) \rangle \end{aligned} \quad (3)$$

185 Finally, mean solar radiation input, horizontal Ekman advection and horizontal non-Ekman
 186 advection were evaluated explicitly from data available at each grid point of the test area (see
 187 subsections 2.4.1, 2.4.2, 2.4.3 respectively). Similarly, the mean vertical Ekman advection could
 188 be estimated by evaluating a vertical Ekman velocity w_e from the wind-stress curl at each grid
 189 point and from the modeled area mean temperature $\langle T \rangle$ (see subsection 2.4.4). The mean vertical
 190 diffusion term $\partial_z \langle K \rangle \partial_z \langle T \rangle$ was computed directly by the 1D model and the upper boundary
 191 conditions, i.e., the surface fluxes, at each grid point (see subsection 2.4.1). The term including
 192 correlations of vertical diffusion ($\partial_z \langle K'' \partial_z T'' \rangle$) was parameterized (see subsection 2.4.5) since
 193 no data could provide an evaluation of this term across the test area. The vertical non-Ekman
 194 advection term $-\langle w_{ne} \partial_z T \rangle$ and the three subgrid-scale terms: correlations in the solar
 195 penetration $\frac{\langle F_{sol}'' \partial_z T'' \rangle}{\rho_0 C_p}$, correlations of the fluctuations of the vertical velocity and temperature
 196 $\langle w_e'' \partial_z T'' \rangle$ and horizontal tracer diffusion due to small turbulent scales $\langle \nabla_h \cdot (\overline{T'' \vec{u}''}) \rangle$ are weak and
 197 were supposed to be negligible.

198 2.3. Setup

199 To implement the inverse method, a simulation test area was chosen, large enough to minimize
 200 the impact of horizontal advection, but not too much so that the hydrology, water properties and
 201 bottom topography are not too heterogeneous. The area displayed in Figure 1 indicates an
 202 homogeneous bottom topography, and includes the wintertime NWM deep convective patch
 203 [e.g., *Herrmann et al.*, 2009; *Houpert et al.*, 2016]. The simulation domain covers a surface area
 204 of about 300 x 300 km² but the surface flux correction can be applied on a wider area, i.e., the
 205 whole domain area represented in Figure 1. As indicated in Figure 1, the LION buoy, anchored
 206 at 4.703°E 42.102°N, lies inside the test area, while the AZUR buoy anchored at 7.83°E 43.38°N
 207 lies in the outer domain. The LION and AZUR buoys have been providing atmospheric and
 208 oceanic observables since 2001 and 1999 respectively; these data were used for evaluation of the
 209 adjusted fluxes in subsection 4.1.

210



211

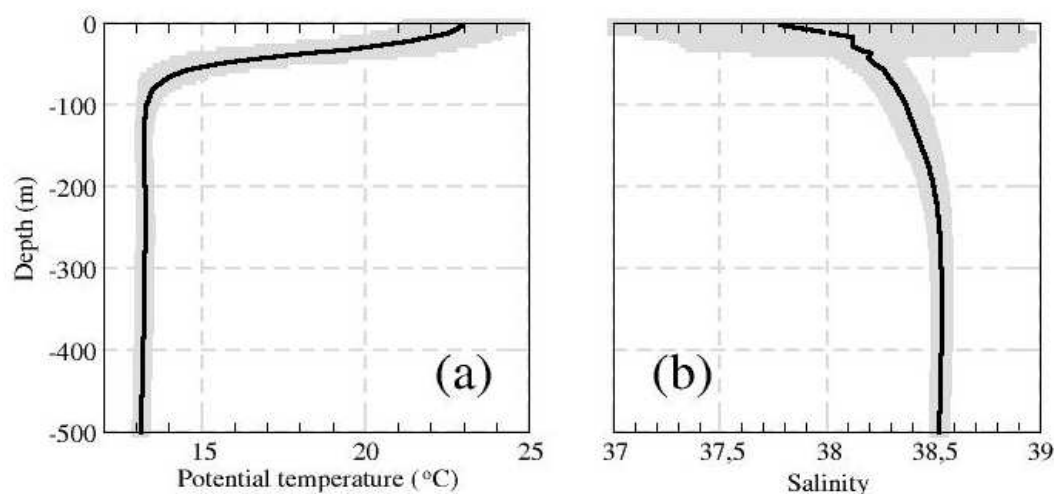
212 **Figure 1.** Bathymetry (m) of the north-western Mediterranean. The black box corresponds to the
 213 test area. The 89 CTDs of the MOOSE 2012 hydrological survey (from 2012/07/24 to
 214 2012/08/08) are represented by red dots, the ship trajectory by yellow lines and the position of
 215 the anchored AZUR and LION buoys by black circles.

216 The method was applied during one seasonal cycle from 2012/08/01 to 2013/07/31, by using
 217 most of the data collected in the test area during six hydrological surveys: MOOSE 2012 and
 218 MOOSE 2013 (respectively from 2012/07/24 to 2012/08/08 with 89 CTD casts and from
 219 2013/06/13 to 2013/07/09 with 77 CTD casts), DeWEX-1 (from 2012/08/22 to 2012/09/06 with
 220 54 CTD casts) and DeWEX-2 (from 2013/04/05 to 2013/04/24 with 73 CTD casts), as well as
 221 the HyMeX-SOP1 in autumn 2012 [Ducrocq *et al.*, 2014] and HyMeX-SOP2 in winter 2013
 222 [Estournel *et al.*, 2016a]. We also used various in-situ data (gliders, ARGO floats, surface
 223 drifters, moored buoys) and satellite platforms, either for initialization of the SCM (see below),
 224 or for calculating the cost function (subsection 2.5). As mentioned in the introduction, the more
 225 numerous the data, stronger is the constraint on the realism of the numerical simulations and
 226 finally on the adjusted fluxes.

227 During the same period, operational and research oceanic models were run and some of their
 228 outputs were used. For estimating large scale geostrophic advections of temperature and salinity

229 as well as horizontal Ekman advection of salinity, we used outputs of the operational
230 MERCATOR PSY2V4R4 model [Drillet *et al.*, 2014] (see subsections 2.4.2 and 2.4.3).
231 Moreover, for evaluating the heat budget closure presented in subsection 4.3, the MEDRYS
232 reanalysis [Hamon *et al.*, 2016] and some outputs of the mesoscale research SYMPHONY
233 [Marsaleix *et al.*, 2009, 2012] and MARS3D [Garreau *et al.*, 2011] models were also used. The
234 MEDRYS reanalysis, based on the MERCATOR assimilation system, assimilated numerous in-
235 situ data collected between 2007 and 2013 in the NWM. Unlike MERCATOR and MEDRYS,
236 the SYMPHONY and MARS3D models do not assimilate altimetry nor in-situ data. They were
237 initialized either from MERCATOR fields (MARS3D) or from a mixed of in-situ data and
238 MERCATOR outputs (SYMPHONY) [Estournel *et al.*, 2016b] and forced with fluxes derived
239 from NWPM fields.

240 The SCM was initialized with 35 CTDs (over 89) collected in the test area during the MOOSE
241 2012 campaign (Figure 1). The mean temperature and salinity profiles were linearly interpolated
242 on a 5 m regular vertical grid before spatial averaging (Figure 2). The profiles were used as
243 initial state at the central time of the survey (i.e., 2012/08/01). The mean potential temperature
244 profile (Figure 2a) is homogeneous from 2800 m to 100 m due to the presence of WMDW, and
245 covered by well stratified surface waters above 100 m. The mean salinity values (Figure 2b)
246 range between 38.3 and 38.6 from the bottom to about 200 m and exhibit a maximum value of
247 38.6 near 400 m. Above, salinity drops sharply near the surface to 37.8. Both mean temperature
248 and salinity profiles display substantial spatial variability near the surface, which rapidly
249 decreases with depth (Figure 2).



250

251 **Figure 2.** (a) Area mean temperature (in °C) and (b) salinity profiles from the CTDs collected
 252 within the test area (see Figure 1) during the MOOSE 2012 hydrological network with standard
 253 deviations in grey.

254

2.4. Forcings

255

2.4.1. Surface Flux Guess

256 To force the SCM, the flux guess was computed after collecting several surface meteorological
 257 and oceanic variables. One of the objectives being to take into account oceanic mesoscales in the
 258 surface fluxes, we chose SST fields produced operationally since 2010 by the Centre de
 259 Météorologie Spatiale (Météo-France, Lannion), at a daily frequency and analyzed and
 260 positioned on a ultra-high resolution 0.02° longitude x 0.02° latitude grid. This production is
 261 issued from the MEDSPIRATION project ([http://cersat.ifremer.fr/thematic-
 262 portals/projects/medspiration](http://cersat.ifremer.fr/thematic-portals/projects/medspiration)) funded by the European Space Agency (ESA). The atmospheric
 263 variables (air temperature, humidity, sea level pressure and surface winds) come from the
 264 operational Météo-France AROME model [Bouttier, 2007]. Its outputs were available every hour
 265 on a 0.025° longitude x 0.025° latitude grid and were interpolated on the finer SST grid. Rather
 266 than using precipitation from the AROME-France model, we preferred to download TRMM
 267 precipitation fields [Huffman *et al.*, 2007], because precipitating clouds or cells are better
 268 positioned than in models [Béranger *et al.*, 2006; Pfeifroth *et al.*, 2013], even if the calibration of
 269 satellite precipitation over oceans and seas can still be improved [Serreze *et al.*, 2005;]. As

270 TRMM data were available every three hours on a 0.125° longitude x 0.125° latitude grid, the
 271 fields were linearly interpolated every hour at the resolution of the SST grid. The daily SST
 272 fields were also interpolated every hour. Finally, the COARE3.0 bulk algorithm [Fairall *et al.*,
 273 2003] was used to produce hourly turbulent fluxes (latent and sensible heat fluxes and wind-
 274 stress) on the 0.02° longitude x 0.02° latitude SST grid.

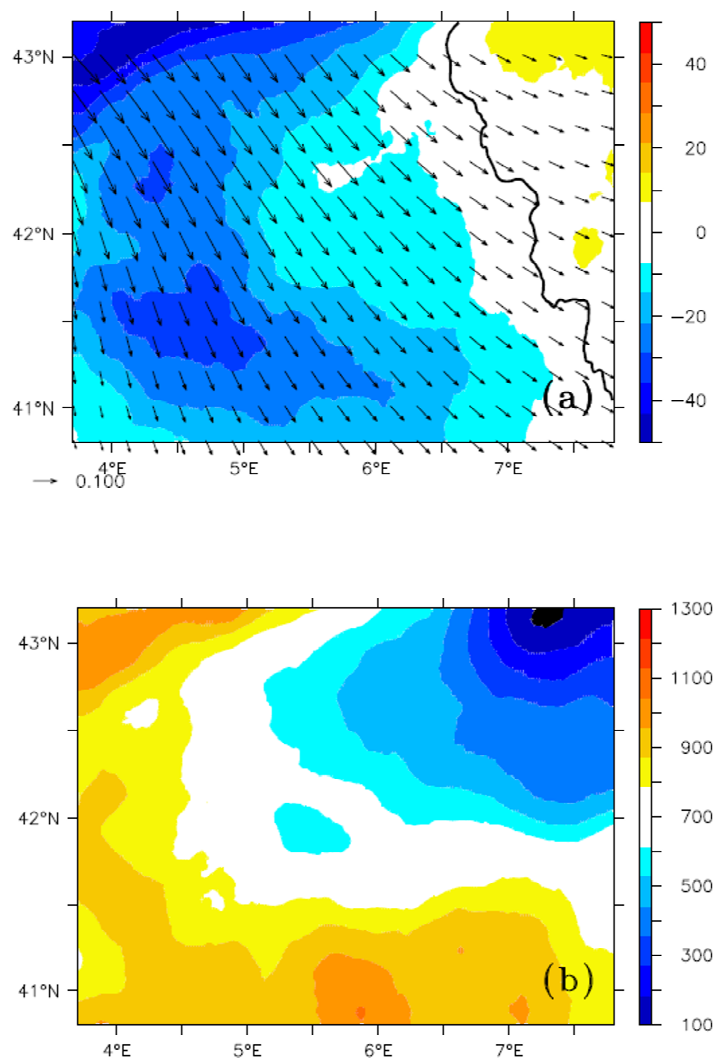
275 The radiative fluxes (incoming longwave and shortwave radiations) were downloaded from the
 276 Centre de Météorologie Spatiale (Météo-France, Lannion), where they are produced
 277 operationally at a time frequency of one hour on a regular grid of 0.05° longitude x 0.05° latitude
 278 [Brisson *et al.*, 1999, 2001]. These data are compared operationally with moored buoys [Le
 279 Borgne *et al.*, 2007] and sometimes with ship data during dedicated experiments at sea [e.g.,
 280 Eymard *et al.*, 1999; Caniaux *et al.*, 2005a]. They provide interesting comparisons with biases
 281 less than 2 W m^{-2} and root mean squares ranging from 10 to 20 W m^{-2} (except in some specific
 282 cases of Saharan dust aerosols). Their good performance against in-situ data imply that they
 283 don't need to be corrected by the optimization procedure of the inverse method. Like the other
 284 flux-relative variables, the radiative fluxes were interpolated on the SST grid. The net longwave
 285 radiation F_{LW} was computed from the incoming longwave radiation F_{DLR} and SSTs with the
 286 classical expression:

$$287 \quad F_{LW} = (1 - \alpha)F_{DLR} - \varepsilon\sigma(SST + 273.16)^4 \quad (4)$$

288 with a longwave reflectance $\alpha = 0.045$ [Bignami *et al.*, 1995], an emissivity $\varepsilon = 0.97$ and a
 289 Stefan-Boltzmann constant $\sigma = 5.67 \times 10^{-8} \text{ W m}^{-2} \text{ K}^{-4}$. For the net shortwave radiation an albedo
 290 of 0.055 was adopted.

291 The mean annual surface net heat flux and wind-stress are shown in Figure 3a. The area mean
 292 net heat flux is negative (-14.3 W m^{-2}), meaning cooling for the sea. Actually, the area is
 293 straddling the zero flux line located on the eastern part of the domain (thick black line in Figure
 294 3a). The area with the lowest heat fluxes corresponds to the area of maximum wind-stress
 295 associated with the dominant north-northwesterly continental winds (i.e., the northerly Mistral
 296 and north-westerly Tramontane blowing down the Rhône and Garonne river valleys). Figure 3b
 297 represents the mean annual E-P budget during the same period. The area mean value is 711 mm
 298 yr^{-1} . A belt of higher values is present to the west of the domain, where the strongest winds

299 generate higher evaporation rate, and farther south with values up to 1000 mm yr^{-1} on the warm
 300 waters of the Balearic front. The north-eastern portion of our study region has a much lower E-P
 301 budget ($\sim 100 \text{ mm yr}^{-1}$) attributable to intense precipitation, which mainly affects the Gulf of
 302 Genoa during the winter period (associated with the famous Genoa low).



303
 304 **Figure 3.** Map of the year mean (from 2012/08/01 to 2013/07/31) guess for : (a) the surface net
 305 heat fluxes (shades, units W m^{-2}) with zero isoline in black and wind-stress every 10 grid point
 306 (arrows, units N m^{-2} and scale in the lower left corner); (b) evaporation minus precipitation (mm
 307 yr^{-1}).

308 **2.4.2. Horizontal Ekman Advection**

309 We assumed that the horizontal Ekman advection of temperature could be calculated from
 310 satellite SSTs and wind-stress fields. This hypothesis is reasonable because the depth of the
 311 Ekman layer is relatively low during most time of the year in the area and less than the mixed
 312 layer depth, so that over this depth, the temperature profiles were assumed homogeneous to be
 313 taken as SST. The horizontal advection term in equation (3) was thus computed every hour and
 314 at the same spatial scale as the surface fluxes, from the following classical expression:

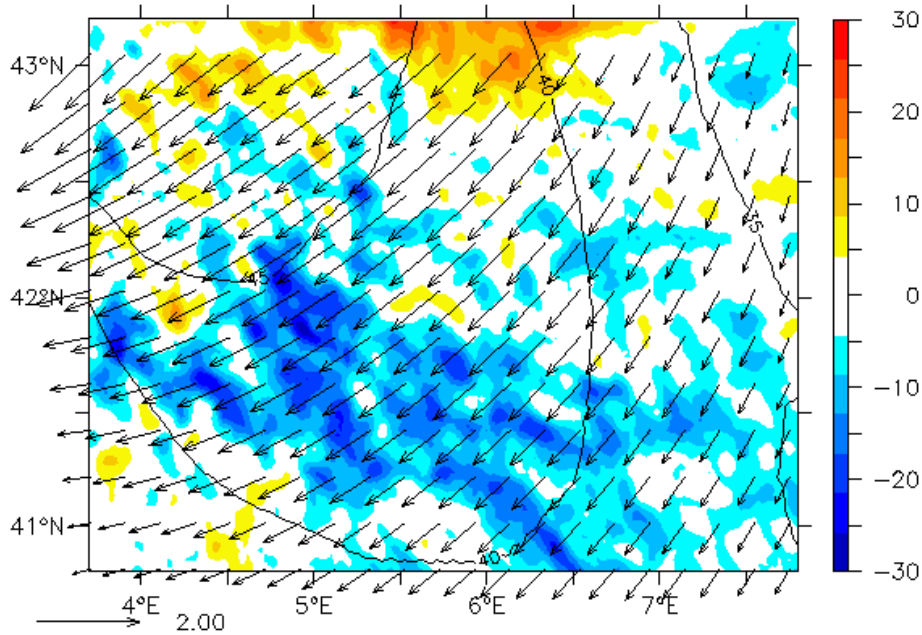
$$315 \quad -\vec{u}_e \cdot \vec{\nabla}_h T = -\frac{1}{\rho_0 f} (\vec{k} \times \vec{\tau}) \cdot \vec{\nabla}_h SST \quad (5)$$

316 where \vec{k} is the unit vertical vector, $\vec{\tau}$ the wind-stress and f the Coriolis parameter. According to
 317 *Cushman-Roisin* [1987], the Ekman layer depth could be computed from the turbulent velocity
 318 as:

$$319 \quad h = 0.4 \frac{u_*}{f} \quad (6)$$

320 with $u_* = \sqrt{\frac{|\vec{\tau}|}{\rho_0}}$. A similar formulation was used for the horizontal Ekman advection of salinity,
 321 in which the SSS values were taken from the MERCATOR PSY2V4R4 model and linearly
 322 interpolated every hours on the same spatial grid as SSTs. In the SCM, horizontal Ekman
 323 advection was added as an external forcing term on the thickness of the Ekman layer h .

324 Figure 4 represents the annual mean horizontal Ekman advection of temperature, superimposed
 325 with the Ekman transport and Ekman layer depth. Over the whole area, the Ekman transport is
 326 southwestward, perpendicular to the dominant surface wind-stress. The mean annual transport of
 327 temperature is quite noisy, with predominantly positive values in the north and negative values in
 328 the south. This configuration, far from reflecting the mean transport of the time mean SST field
 329 by the time mean current, reflects the predominant role of the eddy field. The mean annual depth
 330 of the Ekman layer, with values ranging from 35 to 50 m, is deeper in the north-western part of
 331 the domain due to the influence of the dominant winds.



332

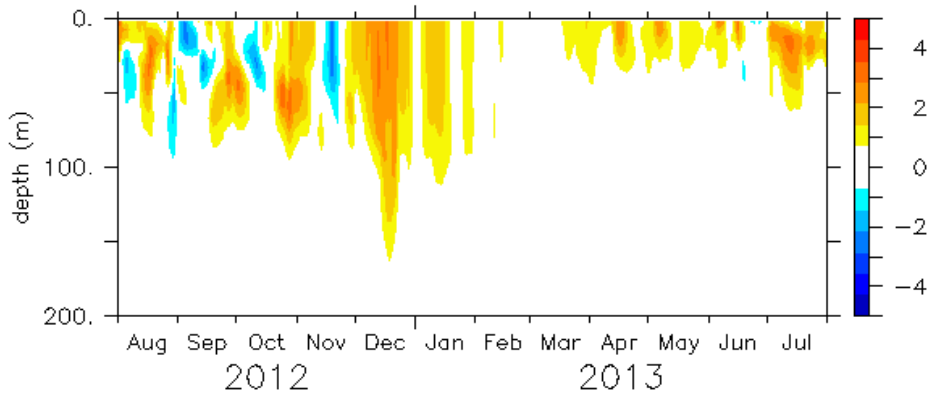
333 **Figure 4.** Same as Figure 3 for the horizontal Ekman advection of temperature (shades, units 10^8 $^{\circ}\text{C s}^{-1}$), Ekman transport (arrows, units $\text{m}^2 \text{s}^{-1}$ and scale in the lower left corner) every 10 grid
 334 point and Ekman depth (contours, units m).
 335

336 2.4.3. Horizontal Non-Ekman Advection

337 For the horizontal non-Ekman advection, we used geostrophic advectons derived from the
 338 MERCATOR PSY2V4R4 model. This model assimilates altimetry, suggesting that the large-
 339 scale circulation in the NWM is better constraints than in models without assimilation.
 340 Moreover, many comparisons were done with MARS3D and SYMPHONIE models and with
 341 MEDRYS reanalysis during winter 2012-2013 in the NWM (not shown). These comparisons led
 342 us to conclude that the MERCATOR model responds quite well to our needs for reconstructing
 343 geostrophic advectons over the whole water column.

344 The seasonal evolution of the mean temperature geostrophic advection versus depth is presented
 345 in Figure 5. The plot confirms that advectons are the strongest in the surface layers down to a
 346 depth of about 150 m. From January to March, geostrophic advectons were weaker than during
 347 the rest of the year because during this period intense cooling significantly reduced horizontal
 348 gradients of temperature and salinity across the area, despite the intensification of the rim-

349 current. During the rest of the year, alternatively warm and cold subsurface advctions reflect the
 350 presence of mesoscale features (eddies and filaments) mainly transiting along the Balearic Front
 351 around 40°N. At the surface and after one annual cycle, geostrophic advection tends to warm
 352 SSTs and freshen SSSs in the test area.



353

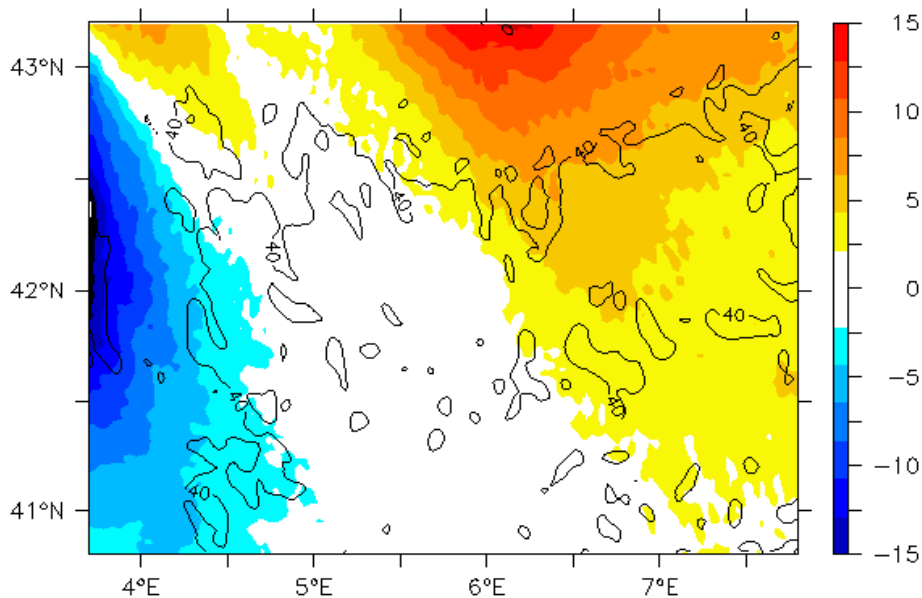
354 **Figure 5.** Temporal evolution of the domain average geostrophic advection of temperature (10^7
 355 $^{\circ}\text{C s}^{-1}$) as a function of depth (m).

356 2.4.4. Vertical Ekman Advection

357 At any point of the test area and at each time step, a vertical Ekman velocity w_e was evaluated
 358 from the wind-stress curl and then averaged over the test area. For computing vertical advctions
 359 of temperature and salinity, we must further impose a vertical profile for $\langle w_e \rangle$. As in *Caniaux et*
 360 *al.* [2005b], we chose zero at the surface, maximum at the Ekman layer depth, and decreasing to
 361 zero at the bottom of the water column. In the SCM, vertical Ekman advctions were calculated
 362 at each level of the SCM from vertical gradients of temperature and salinity and from the vertical
 363 profile of $\langle w_e \rangle$ with an upstream numerical scheme compatible with the other schemes of the
 364 model.

365 The mean annual Ekman pumping is displayed in Figure 6. An ascending positive (subsiding
 366 negative) pumping zone is present on the right cyclonic (left anticyclonic) side of dominant
 367 winds. The two areas of opposite sign are separated by a nearly 110 km wide corridor
 368 corresponding to the main pathway of the dominant winds in the area. Note that the patterns of

369 higher and lower pumping values are consistent with the patterns of higher temporal variability
 370 (yearly standard deviations $> 40 \cdot 10^{-6} \text{ m s}^{-1}$). The north-eastern area with positive pumping plays
 371 an important role for preconditioning water masses, by maintaining the doming of isopycnals
 372 inside the gyre interior, as underlined by *Gascard* [1978] and *Madec et al.* [1996] in the Gulf of
 373 Lion or by *Pickart et al.* [2003] in the Irminger Sea, where the Greenland tip jets generate
 374 elevated heat loss and strong wind-stress curl in the lee of Cape Farewell. As the magnitude of
 375 the positive wind-stress curl and its extension are larger than that of the negative pumping zone,
 376 a mean annual positive value is expected in the test area.



377

378 **Figure 6.** Same as Figure 3 for the Ekman pumping (shades, units 10^{-6} m s^{-1}) and temporal
 379 standard deviation (contours, units 10^{-6} m s^{-1}). Contour intervals are $40 \times 10^{-6} \text{ m s}^{-1}$.

380 2.4.5. Subgrid Scale Vertical Mixing

381 This term, symbolized in equation (3) by $\partial_z \langle K'' \partial_z T'' \rangle$, represents a physical process that
 382 increases vertical mixing. As in *Caniaux et al.* [2005b], we suppose that the subgrid scale
 383 fluctuations of this process were due to spatial heterogeneities in the wind field throughout the
 384 test area. To parameterize this process, we considered that the wind-stress was increased by a
 385 factor taking into account the spatial standard deviation σ of the wind magnitude $\langle |\vec{u}| \rangle$, i.e., by

386 multiplying the wind-stress by the factor $\gamma = 1 + \frac{\sigma}{\langle \bar{U} \rangle}$. All year long, the time series of γ displays
 387 a high frequency variability but with no significant trend (not shown). Consequently, a constant
 388 value for this factor was specified to be equal to its mean annual value ($\gamma = 1.34$).

389 2.5. Optimization

390 The optimization of the model simulations needs first to select some adjustable parameters (i.e.,
 391 poorly known constants of the model or constants leading to a great sensitivity to the results) and
 392 to introduce other parameters to correct the surface fluxes. Among the first, two adjustable
 393 constants in the parameterization of the incoming solar penetration were selected because tests
 394 proved that SSTs were very sensitive to R and d_2 in *Paulson and Simpson* [1977]'s
 395 parameterization:

$$396 \quad I(z) = R \cdot \exp\left(-\frac{z}{d_1}\right) + (1 - R) \cdot \exp\left(-\frac{z}{d_2}\right) \quad (7)$$

397 where z is the depth; R denotes a partition parameter between the red and blue-green parts of the
 398 solar radiation spectrum penetrating down to the extinction depths d_1 and d_2 respectively. As the
 399 simulations were quite insensitive to d_1 , the value of the standard type III waters in *Jerlov*
 400 [1976]'s classification was adopted and set to be 1.4 m.

401 Among the second adjustable parameters, five coefficients were introduced in the expressions of
 402 the area mean surface fluxes. These coefficients are supposed to represent corrections to be
 403 brought either to the input parameters or to the exchange coefficients of the bulk formulae:

- 404 1. coefficient β_w corresponds to the errors affecting the surface wind. This parameter plays
 405 an important role because it affects directly wind-stress, latent and sensible heat fluxes,
 406 and horizontal and vertical Ekman advections.
- 407 2. Coefficients β_{ws} and β_l represent the uncertainty affecting the exchange coefficients of
 408 wind-stress and of latent heat flux (and evaporation) respectively. Both are multiplicative
 409 factors.

410 3. For sensible heat flux, a bias β_s was introduced instead of a multiplicative factor, because
 411 sensible heat may frequently change sign in the NWM, air temperatures being frequently
 412 close to SSTs.

413 4. β_p for correcting satellite rainfall.

414 Finally, the corrected fluxes were written as:

$$\begin{aligned}
 \langle \tau \rangle &= \beta_w^2 \beta_{ws} \langle \tau \rangle^* \\
 \langle Q_{lat} \rangle &= \beta_l \beta_w \langle Q_{lat} \rangle^* \\
 \langle Q_{sens} \rangle &= \beta_w \langle Q_{sens} \rangle^* - \beta_s \\
 \langle P \rangle &= \beta_p \langle P \rangle^*
 \end{aligned} \tag{8}$$

416 in which τ stands for the magnitude of the wind-stress, Q_{lat} the latent heat flux, Q_{sens} the sensible
 417 heat flux and P the precipitation, and in which the area mean guess fluxes are affected by a star.
 418 The ranges of values of the seven adjustable parameters are given in Table 1. They were
 419 determined so as to be large enough to be sure to get the optimum, but in reasonable intervals to
 420 discard unphysical solutions.

Parameter (unit)	Range of values	Optimum
R	0.3 – 0.7	0.463
d_2 (m)	5 – 25	20.000
β_w	0.8 – 1.2	1.066
β_{ws}	0.5 – 1.0	0.750
β_l	0.7 – 1.1	0.900
β_s (W m^{-2})	-10 – +10	+4.526

β_p	0.6 – 1.2	1.138
-----------	-----------	-------

421 **Table 1.** *List of adjustable parameters, with their range of values and the optimum obtained with*
422 *the genetic algorithm.*

423 The optimization of the SCM simulations was carried out using a genetic algorithm [Carroll,
424 1996]. This tool is derived from genetics and population evolution. It is used for seeking the
425 extreme of particularly complex functions, sometimes with discontinuities, like in numerical
426 models. The genetic algorithm searches in a N-dimensional space the N parameters that
427 minimize a cost function CF evaluated for each run of the model. In the algorithm, the set of N
428 parameters to be optimized are coded in a binary form called chromosome. The algorithm starts
429 with a randomly chosen population of chromosomes, after which it evaluates the fitness value of
430 each chromosome by computing a cost function, using the corresponding set of parameters to run
431 the model. Then, the three genetic processes of selection, crossover and mutation are performed
432 upon the chromosomes in sequence. During the selection, chromosomes are copied in proportion
433 to their fitness values based on a probability of selection. Crossover acts on the selected
434 chromosomes, using a crossover probability: this operator selects a crossover site within paired
435 strings and exchanges between the two chromosomes the parts located to the right of the
436 crossover site. Lastly, mutation is applied to the chromosomes in order to maintain diversity.
437 After these processes, the new chromosomes are compared to those of the previous generation,
438 and accepted or rejected based on an update probability. The procedure is repeated until
439 convergence or stopped by fixing a maximum number of generations. The output of the
440 algorithm is a set of N optimal parameters obtained after running a generally high number of
441 model simulations (here 50.000). In the present study $N = 7$ for R , d_2 , β_w , β_{ws} , β_l , β_s and β_p .

442 The cost function (CF) is defined as follows:

$$\begin{aligned}
CF = & \alpha_{SST} \sum_i \frac{1}{\sigma_{SST}^2} (\langle SST_{\text{mod}} \rangle - \langle SST_{\text{obs}} \rangle)^2 \\
& + \alpha_{SSS} \sum_j \frac{1}{\sigma_{SSS}^2} (\langle SSS_{\text{mod}} \rangle - \langle SSS_{\text{obs}} \rangle)^2 \\
443 \quad & + \alpha_T \sum_3 \sum_z \frac{1}{\sigma_T^2} (\langle T_{\text{mod}}(z) \rangle - \langle T_{\text{obs}}(z) \rangle)^2 \quad (9) \\
& + \alpha_S \sum_3 \sum_z \frac{1}{\sigma_S^2} (\langle S_{\text{mod}}(z) \rangle - \langle S_{\text{obs}}(z) \rangle)^2 \\
& + \alpha_{RB} \sum_j \frac{1}{\sigma_{RB}^2} (\langle RB_{\text{mod}} \rangle - \langle RB_{\text{obs}} \rangle)^2
\end{aligned}$$

444 In this expression, each term is normalized by the variance σ_k^2 of the series (k refers to the area
445 mean SSTs, SSSs, temperature (T) and salinity (S) profiles and residual buoyancy RB). $\langle SST_{\text{obs}} \rangle$
446 represents the area mean daily satellite SST series (the same as those of the guess fluxes) during
447 the period of simulation ($i = 365$ days). $\langle SSS_{\text{obs}} \rangle$ is the area mean surface salinities obtained from
448 daily objective analyses performed by one of the co-authors [Giordani *et al.*, 2014] during the
449 winter period (i.e., $j = 119$ days) from all the data collected in the NWM (gliders, floats, CTDs,
450 drifters and satellite). For the analyses, temperature and salinity data were first carefully checked
451 to detect any erroneous values. They were then interpolated onto 800 vertical levels (with a 5 m
452 vertical resolution from the surface to the bottom) and objectively analyzed onto a $1/12^\circ$
453 horizontal grid following the procedure used by Giordani *et al.* [2005]. The first guess of the
454 analyses was derived from the operational MERCATOR PSY2V4R4 model. At each grid point,
455 the PSY2V4R4 analysis was corrected with the observations which lie within one influence
456 time/space radius around the grid point, following the procedure of De Mey and Ménéard [1989].
457 A space correlation radius of 10 km, consistent with the mesoscale structures of the NWM, and a
458 decay e-folding time of one day were chosen.

459 In equation (9), $\langle T_{\text{obs}}(z) \rangle$ and $\langle S_{\text{obs}}(z) \rangle$ are the area mean temperature and salinity profiles
460 deduced from CTDs collected during the DeWEX-1, DeWEX-2 and MOOSE 2013 hydrological
461 networks, respectively centered on 2013/02/01, 2013/04/14 and 2013/06/30. Residual buoyancy
462 $\langle RB_{\text{obs}} \rangle$ (units in $\text{m}^2 \text{s}^{-2}$), an integral measure of the stratification of the water column, was

463 computed from the objectively analyzed temperature and salinity fields during the 119 days
 464 period, as:

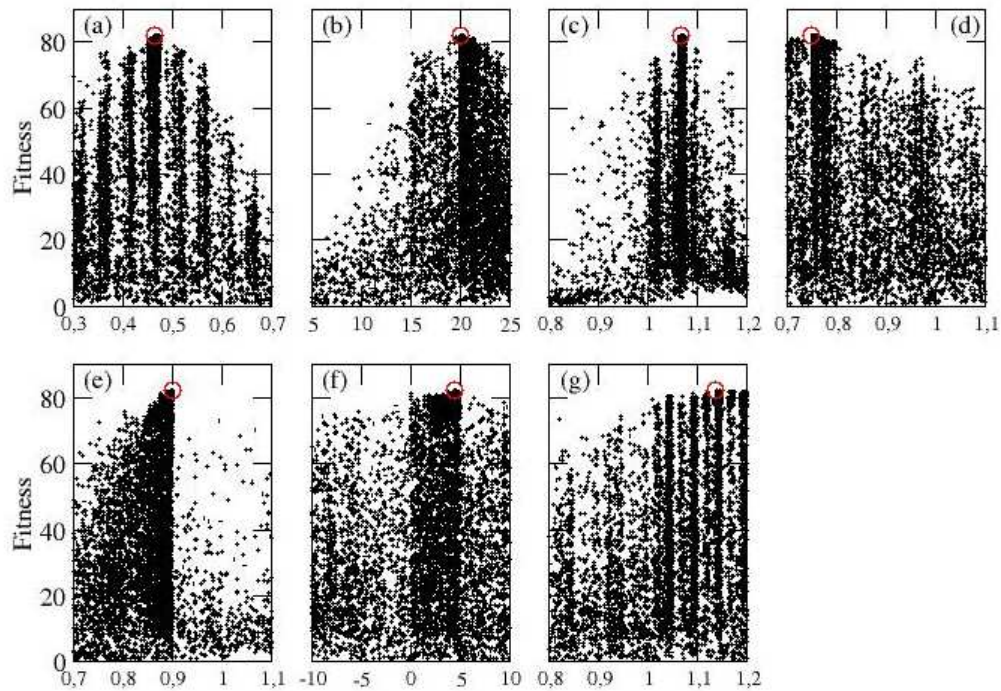
$$465 \quad RB = \int_{-H}^0 zN^2(z)dz \quad (10)$$

466 where $N^2(z)$ is the Brunt-Väisala frequency computed from *McDougall* [1987] and H the depth
 467 of the ocean (2250 m). Finally in equation (9), α_k ($k = 1,5$) are weighting coefficients chosen
 468 inversely proportional to the number of data in the series and function of the confidence we have
 469 in the quality of the data. They were taken as 1, 0.8, 0.1, 0.1 and 0.1 respectively.

470 **3. Results**

471 **3.1. Adjusted Parameters**

472 The optimization with the genetic algorithm was performed after running 50.000 simulations of
 473 the SCM during one annual cycle. For each simulation, the adjustable parameters were chosen by
 474 the genetic algorithm in their preselected range of values (Table 1) and the cost function
 475 computed. In Figure 7, the fitness function (10000 times the inverse of the function cost) is
 476 plotted against the value of each adjustable coefficient. Each black point corresponds to the
 477 fitness value evaluated for each simulation and the red circle is the maximum fitness function.
 478 The latter provides the optimal adjustable set of coefficients, which also figure in Table 1.



479

480 **Figure 7.** Fitness function for each adjustable parameter: (a) R , (b) d_2 , (c) β_w , (d) β_{ws} , (e) β_l , (f)
 481 β_s , (g) β_p . The maximum fitness values are circled.

482 The optima for R and d_2 (Table 1 and Figure 7a-b) are close to the values in *Jerlov* [1976]’s
 483 classification, although R appears slightly underevaluated compared to type III waters. However,
 484 the adjusted values represent a mean annual value for different water types, which may change
 485 during the year and through the area. In Figure 7, sharp peaks of the fitness function correspond
 486 to well identified optimum values. This is the case for the wind coefficient β_w (Figure 7c) and the
 487 latent heat flux coefficient β_l (Figure 7e). Conversely, the sensitivity of the simulations to the
 488 adjustable coefficient is lower for the sensible heat flux coefficient β_s (Figure 7f) and for the
 489 precipitation coefficient β_p (Figure 7g) for which the values of the fitness function form almost a
 490 plateau.

491 In Table 1, the optimum of β_w means that the wind needed to be slightly increased by a factor of
 492 1.066, for optimizing both the wind-stress, the latent (as well as evaporation) and sensible heat
 493 fluxes, the horizontal and vertical Ekman advections. On the other side, the optimum of β_{ws}
 494 (supposed to correct the exchange coefficient of the wind-stress) being 0.75 means that the guess
 495 wind-stress was largely overestimated and according to equation (8) had to be reduced by a final

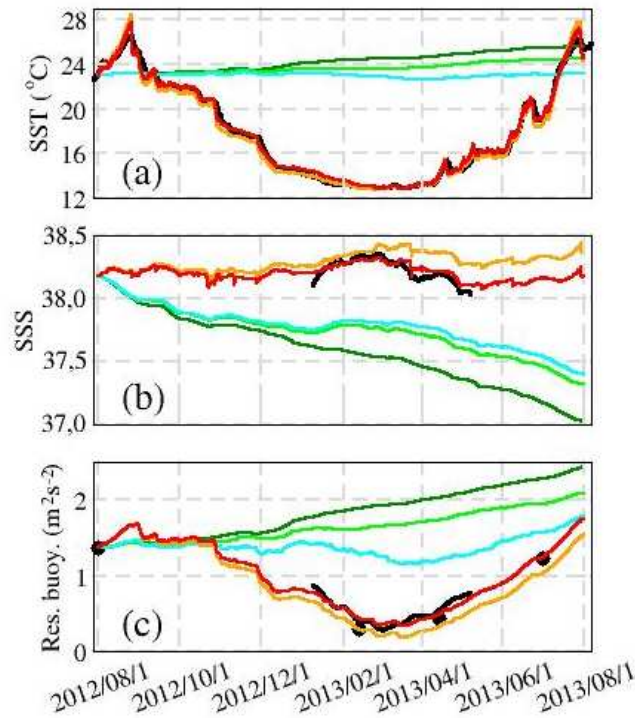
496 factor of $0.75 \cdot 1.066^2 = 0.85$. Similarly, the exchange coefficient of the latent heat flux had to be
 497 multiplied by a factor of 0.9 and the guess flux by a factor of $0.9 \cdot 1.066 = 0.96$. Note that the
 498 TRMM precipitation fields were underestimated by an factor of 1.138 for adjusting the model
 499 near surface salinity. Accordingly, when the flux correction is applied to each grid point of the
 500 test area with equation (8), and during one annual cycle the mean latent and sensible heat fluxes
 501 were reduced by 4.7 and 3.5 $W m^{-2}$ respectively (Table 2); this led to an increase of the net heat
 502 flux by 8.2 $W m^{-2}$. Similarly, the adjusted E-P balance is reduced by 163 $mm yr^{-1}$, due to an
 503 overestimation of evaporation (60 $mm yr^{-1}$) and an underestimation of precipitation (103 $mm yr^{-1}$)
 504 of the guess. The average value of the adjusted wind-stress is lowered by about 0.02 $N m^{-2}$.

Flux	Guess	Adjusted	Difference guess-adjusted
Sensible heat flux	-16.4	-12.9	-3.5
Latent heat flux	-113.8	-109.1	-4.7
Net heat flux	-14.3	-6.1	-8.2
Wind-stress	0.156	0.133	0.023
E	1460.8	1400.9	59.9
P	749.3	852.3	-103.0
E-P	711.5	548.6	162.9

505 **Table 2.** Comparison of guess and adjusted mean annual fluxes. Domain considered: $3.71^{\circ}E$ -
 506 $7.79^{\circ}E - 40.31^{\circ}N-42.69^{\circ}N$; period considered: 2012/08/01 to 2013/07/31. Heat fluxes are in W
 507 m^{-2} , wind-stress in $N m^{-2}$ and water fluxes in $mm yr^{-1}$.

508 3.2. The Optimized Simulation

509 We now compare the evolution of the area mean satellite SST, reanalyzed SSS and residual
510 buoyancy evolutions (considered as our reference) with the model simulations after introducing
511 successively first the three advection terms (geostrophic advection, horizontal Ekman advection,
512 vertical Ekman advection), then the surface fluxes and finally the adjusted surface fluxes. Figure
513 8 displays the contribution and order of magnitude of each process during one annual cycle and
514 how the simulations of SST, SSS and residual buoyancy are improved with the adjusted fluxes.
515 Satellite SSTs present a significant seasonal cycle with a peak to peak amplitude of 15°C (black
516 curve in Figure 8a). The annual cycle is flattened in winter because SSTs never fall below
517 12.8°C when the mixed layer is deep. Some marked cooling events punctuated the seasonal cycle
518 in autumn (e.g., in early December) and some warming events in spring (e.g., mid-April and
519 mid-June) in response to intense surface fluxes. After introducing geostrophic advection alone
520 (dark green curve in Figure 8a), the SST series is marked by a regular warming with a final
521 yearly gain of 2.6°C. When adding horizontal Ekman advection (green curve in Figure 8a), the
522 SST trend drops to about 1°C, while with vertical Ekman advection (cyan curve) the yearly trend
523 is reduced to zero. Obviously, the surface flux is the main process, which allows to reconstruct
524 the annual cycle and the intraseasonal warming and cooling short events (orange curve in Figure
525 8a). Remarkably, the modeled SST series obtained with the adjusted fluxes (red curve) is quite
526 close to the daily satellite SST series, with a bias of 0.011°C (0.06 %) and a mean standard
527 deviation of the differences between the two series of 0.017°C.



528

529 **Figure 8.** Temporal evolution of (a) SST ($^{\circ}\text{C}$), (b) SSS and (c) residual buoyancy ($\text{m}^2 \text{s}^{-2}$)
 530 simulated by the model, when activating only geostrophic advection (dark green curve), then
 531 successively adding horizontal Ekman advection (green), vertical Ekman advection (cyan),
 532 surface fluxes (orange), and when using the adjusted surface fluxes (red curve). The black curves
 533 correspond to the reference (a) mean satellite SSTs, (b) analyzed SSSs from in-situ data during
 534 the period 2013/01/09 to 2013/05/07 and (c) residual buoyancy (computed from the 3D analyses
 535 during the same period). The black points correspond to the residual buoyancy calculated from
 536 the CTDs collected in the test area during MOOSE 2012 (median date 2012/08/01), DeWEX-1
 537 (2013/02/13), DeWEX-2 (2013/04/14) and MOOSE 2013 (2013/06/30).

538 For SSSs, our reference is the analyzed wintertime series (see subsection 2.5). SSS values range
 539 from 38.04 to 38.36 with a maximum reached in late February 2013 (black curve in Figure 8b).
 540 By introducing geostrophic advection, SSS undergoes a strong but quite steady decrease of 1.2
 541 unit after one year (dark green curve in Figure 8b). Horizontal Ekman advection reduces the
 542 yearly trend and introduces seasonal variability in autumn and winter (green curve). Vertical
 543 Ekman advection generates higher salinity values associated with an import of salinity from
 544 depth and helps to further reduce the negative trend (cyan curve in Figure 8b). With the guess

545 fluxes, the annual range of SSS drops significantly (orange curve in Figure 8b). Finally, with the
546 adjusted fluxes (red curve in Figure 8b), the daily wintertime difference with the analyses falls to
547 0.011 (0.03%) and the standard deviation of the differences between the series to 0.004. Some
548 brief events, that cause sudden SSS drop (e.g., late March, late April), were associated with
549 substantial rainfall. These events are not very well reconstructed by the analyses; the source of
550 this discrepancy must lie in the smoothing effect inherent to the optimal interpolation technique.
551 Note that during the simulation period, SSSs exhibit an overall insignificant negative trend due
552 to the quasi-balance between the surface fluxes and the advection terms, despite a positive input
553 of salinity in January associated with a positive horizontal Ekman advection.

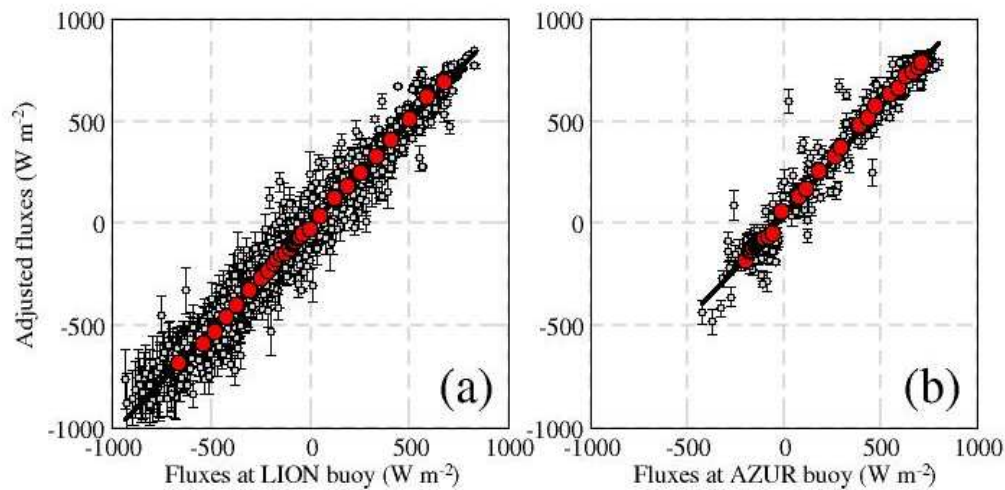
554 The residual buoyancy was evaluated from the wintertime daily temperature and salinity
555 analyses (see subsection 2.5), as well as from CTDs of the four hydrological networks (black
556 curve and black dots in Figure 8c). The residual buoyancy rapidly decreases from mid January
557 2013 and reaches a minimum at the end of February, when the surface area occupied by low
558 stratified waters presents its maximum extension in the test area, after which the residual
559 buoyancy increases during the spring restratification. Geostrophic advection (dark green curve in
560 Figure 8c) produces a marked residual buoyancy increase up to $1 \text{ m}^2 \text{ s}^{-2}$ after one year. The effect
561 of horizontal Ekman advection is to reduce the trend (green curve). Added to horizontal
562 advection, vertical Ekman advection results in the destratification of the water column in winter
563 and restratification in spring (cyan curve). If the Ekman pumping effect was reduced on the SSTs
564 and SSSs series (see Figure 8a-b), its effect on residual buoyancy, thus on the seasonal cycle of
565 the upper top 300 m, is obvious. After introducing the surface fluxes, the peak to peak annual
566 cycle is enhanced (orange curve in Figure 8c). Finally, the effect of the adjusted fluxes is
567 striking: the bias between the model and analyzed series falls to $-0.029 \text{ m}^2 \text{ s}^{-2}$ and the standard
568 deviation of the difference to $0.005 \text{ m}^2 \text{ s}^{-2}$. This has the effect of producing a fairly good
569 agreement with the values of the reanalyzed MOOSE 2013 network (red curve) after almost one
570 seasonal cycle.

571 **4. Evaluations**

572 **4.1. Comparison With Fluxes at the LION and AZUR Buoys**

573 The adjusted fluxes were calculated over a larger area than the test area (0°E-12°E, 38°N-
574 44.5°N; see Figure 1), i.e., the simulation domain of the operational Météo-France AROME
575 model over the Mediterranean Sea. However, the spatial resolution was reduced to a grid of
576 0.04° longitude x 0.04° latitude to avoid spatial interpolations near the coast. The calculation was
577 performed by applying equation (8) at each grid point of the large domain area, every hour and
578 during one year (2012/08/01 – 2013/07/31). In this section, we evaluated the adjusted fluxes
579 locally, through their comparison with the in-situ data collected at the LION and AZUR buoys
580 (see locations in Figure 1). The buoy datasets include radiative fluxes (incoming longwave and
581 shortwave radiations) and all the near-surface meteorological observables needed to estimate the
582 turbulent fluxes, except precipitation. Previously, the variables downloaded from the HyMeX
583 website were scrupulously checked. Out-of-range values were cleaned and sequence values
584 deemed to be unreliable or displaying periods of constant values were rejected. The data were
585 then placed on a regular, hourly temporal grid, and isolated missing data or short sequences of
586 missing data were linearly interpolated from adjacent ones. Compatibility between relative
587 humidity and dew-point measurements was checked and corrected if necessary (for example,
588 dew-point values could excess air temperatures, under high humidity or saturated conditions).
589 Finally, because of missing sequences and rejected data, only 1818 and 514 hourly fluxes (over
590 8760) were available at the LION and AZUR buoys respectively for the comparison.

591 Moreover, for comparing the adjusted and the buoy net heat fluxes, we preferred to use several
592 bulk algorithms instead of selecting only one, due to errors affecting bulk formulae. For that, we
593 selected seven bulk formulae, established over various oceanic basins of the world ocean, i.e.,
594 *Anderson* [1993], *Brut et al.* [2005], *Fairall et al.* [2003], *Dupuis et al.* [2003], *Persson et al.*
595 [2005], *Caniaux et al.* [2005a] as well as *Smith* [1980], whose wind-stress parameterization was
596 associated with *De Cosmo et al.* [1986] for the latent and sensible heat fluxes. Figure 9
597 represents the scatter plots at the two buoys of the adjusted net heat flux series versus the median
598 of the seven net heat flux estimates, as well as their inter-quartile range (IQR hereafter).



599

600 **Figure 9.** Scatter (grey points) and Q-Q (red points for the 30-quantiles) plots comparing the
 601 adjusted fluxes with the surface net heat fluxes estimated from in-situ measurements: (a) at the
 602 LION ($N = 1818$; $r^2 = 0.96$) and (b) AZUR buoys ($N = 514$; $r^2 = 0.96$). The turbulent fluxes were
 603 evaluated with 7 bulk formulae and the medians of each of the 7 estimates are plotted with their
 604 inter-quartile range represented by bars. The comparison covers the period 2012/08/01 to
 605 2013/07/31.

606 The net heat flux at the buoys is predominantly governed by turbulent heat flux and solar
 607 radiation and its sign depends on the seasonal balance between net solar radiation and latent heat
 608 flux. At the LION buoy (Figure 9a), the range of the net heat flux is much larger ($\sim 1700 \text{ W m}^{-2}$)
 609 than at the AZUR buoy ($\sim 1200 \text{ W m}^{-2}$) (Figure 9b), a consequence of limited sampling at AZUR
 610 buoy, and in part because the LION buoy is located on the passage of the prevailing stronger
 611 winds with frequent intrusions of cold and dry air from the north. The adjusted and the median of
 612 the in-situ fluxes are in fair agreement ($r^2 = 0.96$ at the two buoys), with only a weak spread of
 613 the data around the first diagonal of the diagram. Note that the IQR of the medians at the two
 614 buoys are much more important at low (negative) than at high (positive) flux values, due to
 615 greater uncertainties in the turbulent heat flux exchange coefficients at high wind, and large
 616 contrast of temperature and humidity between the air and the oceanic surface. The agreement of
 617 the series remains good over the whole range of values with no skew, even for low or high
 618 fluxes, as indicated by the 30-th quantiles of the Q-Q plot (red dots in Figure 9).

619

4.2. Evaluation of NWPM Fluxes

620 In this section, we compare the adjusted fluxes, considered as a reference, with fluxes of four
 621 operational NWPM: the French ARPEGE [Courtier *et al.*, 1991] and AROME [Bouttier, 2007]
 622 models, the NCEP and ECMWF models and one reanalysis, ERA-INTERIM [Dee *and al.*,
 623 2011]. The fluxes of the five products were linearly interpolated on the same horizontal grid
 624 ($0.02^\circ \times 0.02^\circ$) as the adjusted fluxes and compared over the test area. Table 3 provides mean
 625 annual values of the individual flux components of the net heat and water fluxes as well as the
 626 wind-stress, along with the standard deviations.

	ARPEGE	AROME	NCEP	ECMWF	ERA- INTERIM	Adjusted
Sensible heat flux	-23.2 (56.3)	-27.0 (64.3)	-21.4 (55.3)	-17.7 (38.6)	-16.2 (37.2)	-12.9 (34.9)
Latent heat flux	-124.7 (152.8)	-109.0 (127.5)	-118.6 (143.8)	-109.5 (117.8)	-98.9 (105.9)	-109.1 (114.5)
Net longwave	-76.9 (23.8)	-79.6 (22.8)	-77.4 (23.0)	-80.5 (20.5)	-79.0 (21.1)	-66.3 (17.2)
Net shortwave	+172.7 (216.4)	+190.7 (223.2)	+192.7 (228.9)	+184.5 (221.0)	+179.8 (219.1)	+182.2 (266.7)
Net heat flux	-52.1 (317.2)	-24.9 (311.1)	-24.7 (327.0)	-23.2 (284.0)	-14.4 (274.3)	-6.1 (319.4)
Wind-stress	0.143 (0.189)	0.149 (0.202)	0.105 (0.145)	0.145 (0.188)	0.117 (0.148)	0.133 (0.167)
E	1599.8 (1962.1)	1398.7 (1632.5)	1456.4 (1772.4)	1380.9 (1485.5)	1247.5 (1335.4)	1400.9 (1468.5)
P	727.9 (1988.0)	688.1 (2317.4)	731.0 (2098.0)	685.6 (1861.9)	654.6 (1833.0)	852.3 (2851.4)
E-P	871.9 (2625.8)	710.6 (2770.0)	725.4 (2550.5)	695.3 (2280.3)	592.9 (2237.8)	548.6 (3133.5)

627 **Table 3.** Comparison of the operational NWPM: ARPEGE, AROME, NCEP, ECMWF and of the
 628 ERA-INTERIM reanalysis with the adjusted fluxes; standard deviation values in parenthesis.

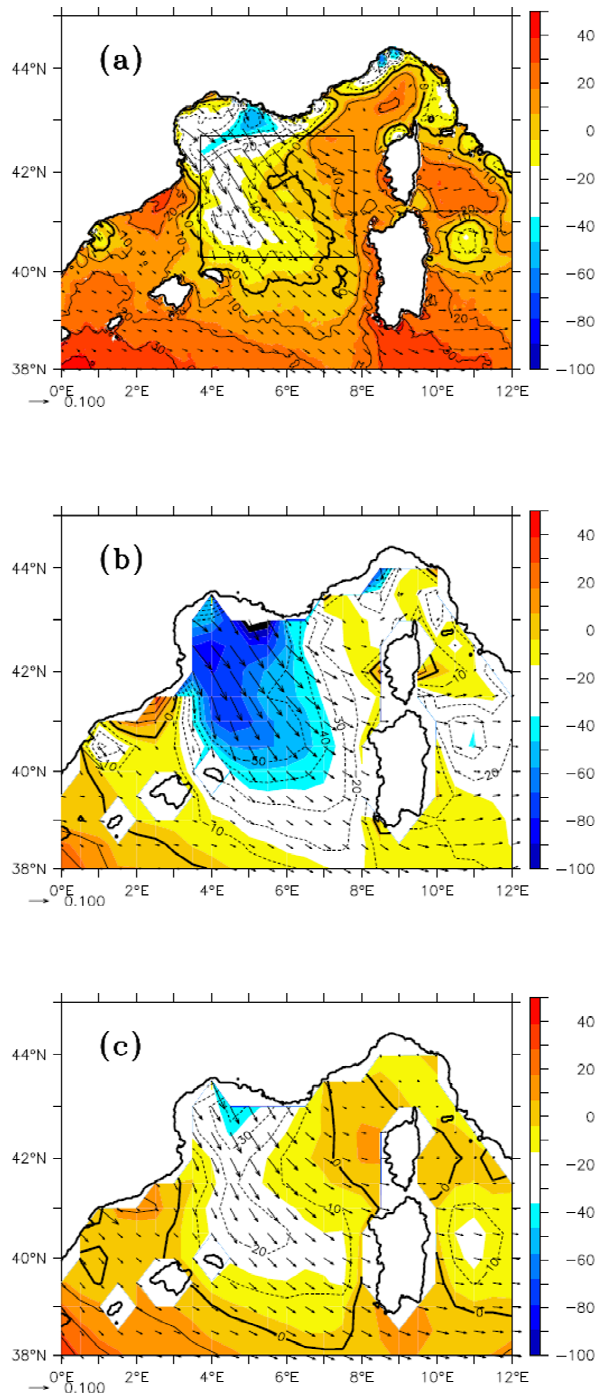
629 *Domain considered: 3.71°E-7.79°E – 40.31°N-42.69°N; period considered: 2012/08/01 to*
630 *2013/07/31. Heat fluxes are in $W m^{-2}$, wind-stress in $N m^{-2}$ and water fluxes in $mm yr^{-1}$.*

631 All model products display a net heat loss by the sea, but they all underestimate the adjusted
632 fluxes, sometimes dramatically like ARPEGE (the difference reaches $40 W m^{-2}$), others weaker
633 like ERA-INTERIM ($8 W m^{-2}$). Note the substantial dispersion between the various NWPM
634 products with a more than twofold intervariation (the range, $38 W m^{-2}$, is of the same order of
635 magnitude as the median, $-25 W m^{-2}$). The model products differ from the adjusted fluxes for
636 different reasons; the differences are primarily the result of differences in either the sensible heat
637 flux for AROME and APREGGE (the heat loss difference exceeds $10 W m^{-2}$), in the latent heat
638 flux for ARPEGE ($< -15 W m^{-2}$) and ERA-INTERIM ($> +10 W m^{-2}$), in the net longwave
639 radiation for the ECMWF and AROME ($< -13 W m^{-2}$), or in the net shortwave radiation for the
640 NCEP ($> +10 W m^{-2}$). On average, the NCEP and ERA-INTERIM underestimate the adjusted
641 wind-stress by $0.028 N m^{-2}$ and $0.016 N m^{-2}$ respectively, while the other products overestimate
642 the adjusted wind-stress over $0.01 N m^{-2}$.

643 The model E-P budgets display a high dispersion (Table 3). Moreover, all NWPM overestimate
644 the adjusted water budget, sometimes radically, with ARPEGE exhibiting the greatest difference
645 with the adjusted fluxes ($323 mm yr^{-1}$). Again, ERA-INTERIM is the model that most agrees
646 with the adjusted fluxes ($44 mm yr^{-1}$), certainly a consequence of a greater amount of data
647 assimilated in the reanalysis. This behavior results from differences in evaporation and from
648 systematic and substantial underestimate of precipitation by the NWPM (the difference with the
649 model mean is $-155 mm yr^{-1}$). All model products underestimate the uncorrected TRMM
650 precipitation as well (not shown). A similar conclusion was reached by *Alhammoud et al.* [2014]
651 who noted that rainfall and specially convective rainfall in ERA-INTERIM over the
652 Mediterranean Sea were systematically underestimated compared to microwave satellite
653 retrievals. The large dispersion between NWPM, both for heat and water fluxes, suggest the
654 importance of errors and drift affecting model runs, when ocean models are forced with
655 atmospheric NWPM flux fields without any corrections [e.g., *Sanchez-Gomez et al.*, 2011;
656 *Valdivieso et al.*, 2015]. Surprisingly, all the model products appreciably underestimate the
657 variability of the satellite shortwave radiation (Table 3) as well as the variability of satellite
658 precipitation compared with adjusted (Table 3) and even with uncorrected TRMM fields (not

659 shown). Consequently, the variability of the E-P budget is also underestimated by all the model
660 products.

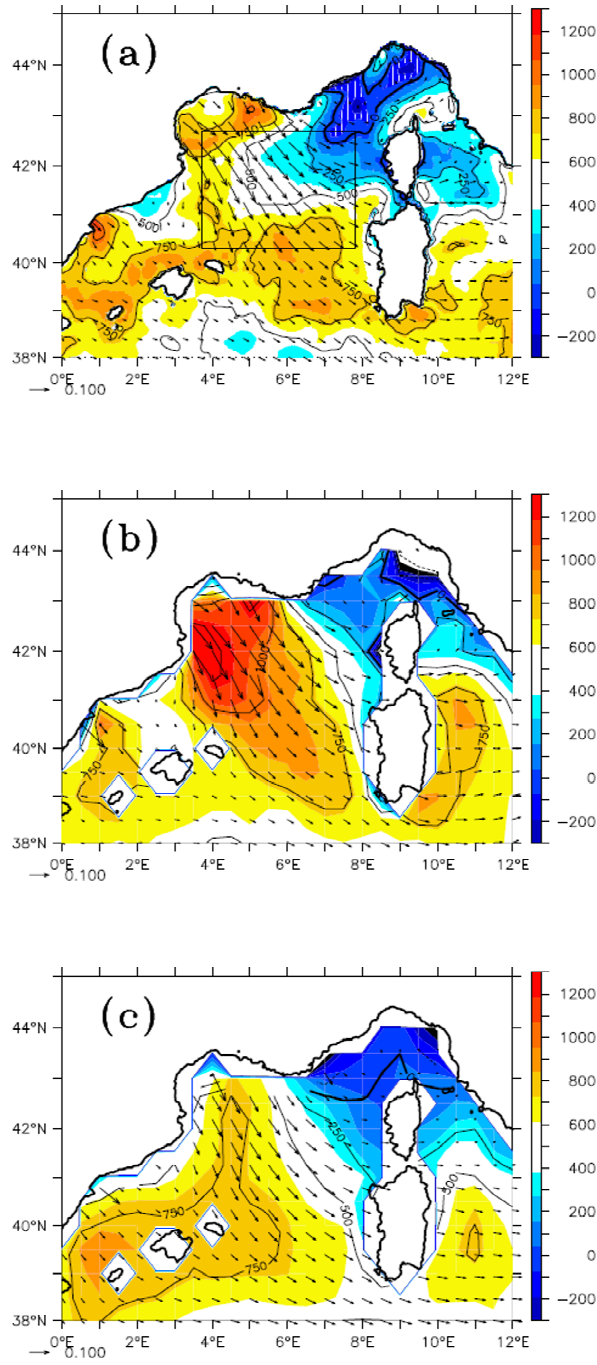
661 Figures 10 and 11 compare the mean annual adjusted flux fields over the larger domain with
662 ARPEGE and ERA-INTERIM fields, respectively the farthest and closest models in comparison
663 with the adjusted fluxes. The spatial patterns of the annual net heat flux (Figure 10) are similar,
664 with heat loss between the Gulf of Lion and Sardinia, reflecting the dominant wind pattern, in the
665 Gulf of Genoa and east of Sardinia. The maximum heat loss ($\sim -60 \text{ W m}^{-2}$) is located in the Gulf
666 of Lion, along the continental margin (Figure 10a). A belt of positive values (heat gain for the
667 ocean of about 10 to 20 W m^{-2}) extends between the southern Pyrenees, the Balearic islands and
668 along the Sardinia and Corsica islands. In both models, the amplitudes differ considerably with
669 the adjusted fluxes with differences reaching locally up to 60 W m^{-2} . In ARPEGE, the zero flux
670 line is hardly present in the vicinity of the Balearic islands (Figure 10b), while in ERA-
671 INTERIM (Figure 10c) the zero flux line delimits a much larger surface area than in the adjusted
672 fluxes.



673

674 **Figure 10.** Maps of the annual net heat flux (shades, $W m^{-2}$) and wind-stress (arrows, $N m^{-2}$ and
 675 scale in the lower left corner) for (a) the adjusted flux dataset, (b) the ARPEGE model, and (c)
 676 ERA-INTERIM. Period considered: 2012/08/01 to 2013/07/31. Contour intervals are $10 W m^{-2}$.
 677 In (a) the wind-stress is represented every 10 grid point.

678 For the water fluxes (Figure 11), the spatial pattern of the adjusted fluxes displays higher values
679 in the Gulf of Lion and from the Balearic to Sardinia islands (750 to 1000 mm yr^{-1}) and much
680 lower values in the Gulf of Genoa, with an excess of precipitation over evaporation rates (Figure
681 11a). The flux fields of the two models present the same longitudinal gradient pattern but with
682 less mesoscale features than the adjusted fluxes (Figure 11b-c), like in the net heat flux fields.
683 The absence of mesoscale features in the NWPM mean annual heat and water flux fields results
684 from the coarser spatial resolution of SST fields used in NWPM. Actually, most of them use the
685 6 km resolution OSTIA analysis [Donlon *et al.*, 2012] which is derived from coarser resolution
686 (mostly satellite) products, which alter the SST and thus the flux mesoscales, compared to the ~ 4
687 km resolution of our flux retrievals based on the ~ 2 km resolution SST product. The ARPEGE
688 model presents an obvious excess of evaporation and stronger wind-stress from the Gulf of Lion
689 to southern Sardinia, while the region of rainfall excess in the Gulf of Genoa is unrealistically
690 underestimated (Figure 11b).



691

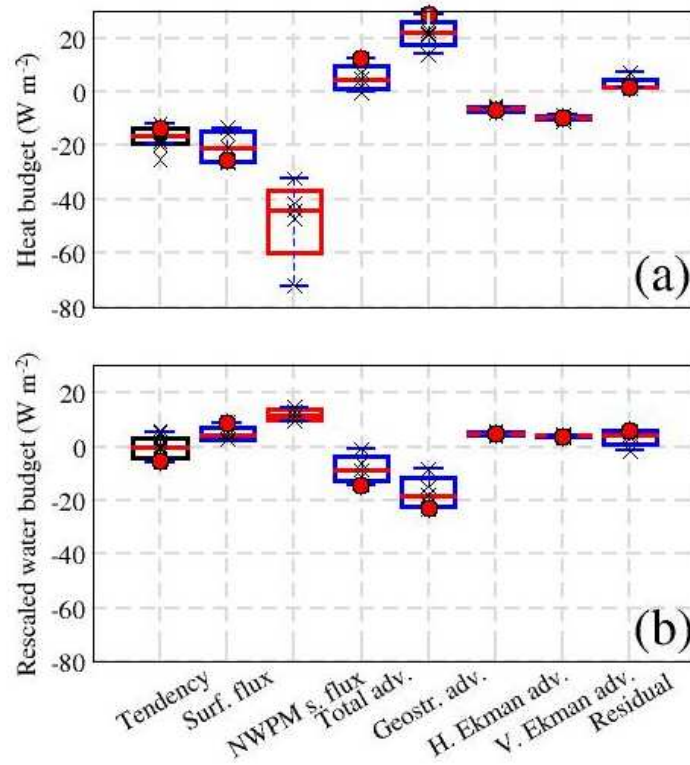
692 **Figure 11.** Same as Figure 10 for the net water flux in mm yr^{-1} . Contour intervals are 250 mm
693 yr^{-1} .

694

4.3. Evaluation of the Heat and Water Budget Closure

695 The objective of this section is to show how the fluxes deduced from the inverse method allows
696 to close the heat and water budgets. A heat budget throughout the water column was performed
697 on the test area between MOOSE 2012 and MOOSE 2013 surveys separated by 333 days. The
698 tendency, surface flux, geostrophic and Ekman advections and a residual were calculated
699 independently, either from in-situ data, or from objective analyses of the CTD networks, or from
700 the ocean models, which were run between the two MOOSE networks. The ocean models
701 include the MERCATOR PSY2V4R4 model, the MEDRYS reanalysis, and the mesoscale
702 models SYMPHONY and MARS3D, as well as the SCM forced with the adjusted fluxes.

703 Each term of the heat and water budgets were computed as box and whisker plots to highlight
704 their contribution and spread (Figure 12). The tendency term was calculated from seven different
705 way: from the mean CTDs collected in the test area during MOOSE 2012 and MOOSE 2013, as
706 well as from objectively analyzed fields deduced from the two hydrological surveys. These
707 analyzed fields were produced exactly like the wintertime temperature and salinity analyses (see
708 subsection 2.5), except that they only include the survey CTDs [Giordani *et al.*, 2014]. Other
709 tendency term estimates were provided by the ocean 3D models, the MEDRYS reanalysis and
710 the SCM. The seven estimates of the tendency term are reported in the first column of Figure
711 12a. The median is negative, meaning cooling of the water column (-16 W m^{-2} with an IQR of 6
712 W m^{-2}). For getting more than one estimate of the adjusted fluxes, four optimization experiments
713 were performed, wherein only the geostrophic advection was changed (i.e., the MERCATOR
714 geostrophic advection was replaced by the MEDRYS, MARS3D and SYMPHONY ones),
715 because this term is estimated to be the main sensitive term and source of errors in our flux
716 retrieval. For these four estimates (second column of Figure 12a), the median is -21 W m^{-2} (IQR
717 $= 12 \text{ W m}^{-2}$), which again corresponds to cooling for the ocean.



718

719 **Figure 12.** Box and whisker plot of the (a) heat and (b) rescaled water budgets (in $W m^{-2}$) in the
 720 test area for the period 2012/08/01 to 2013/06/30 (333 days). From left to right: the black box
 721 represents the lower and upper quartiles of the tendency term (7 estimates); the blue box the
 722 lower and higher quartile of the four flux retrievals obtained after replacing the MERCATOR
 723 geostrophic advection by the SYMPHONY, MARS3D and MEDRYS geostrophic advectons; the
 724 red box corresponds to the five NWPM surface fluxes (ARPEGE, AROME, NCEP, ECMWF and
 725 ERA-INTERIM); the last five blues boxes are the lower and higher quartiles of total advection,
 726 geostrophic advection, horizontal Ekman advection, vertical Ekman advection and the residual
 727 (four estimates each). Each individual estimates are represented by an X; medians are
 728 represented by red horizontal lines, and the maximum and minimum values after discarding
 729 outliers are represented by blue lines joined by blue vertical dotted lines.

730 In the third column of Figure 12a, the surface fluxes of the five NWPM presented and evaluated
 731 in previous subsection are reported. The negative median ($-44 W m^{-2}$), almost three times the
 732 median of the adjusted fluxes ($-16 W m^{-2}$) and the large spread between model fluxes (IQR = 23
 733 $W m^{-2}$, twice the IQR of the adjusted fluxes) are in agreement with the conclusions of the

734 previous section. The total advection terms (column 4 of Figure 12a), i.e., the sum of horizontal
735 geostrophic advections, horizontal and vertical Ekman advections (represented respectively in
736 columns 5, 6, 7), were estimated with the geostrophic advections of the ocean models and the
737 horizontal and vertical Ekman advections derived from the flux guess corrected with the adjusted
738 coefficients of equation (8). The positive median value of total advection (22 W m^{-2}) is the result
739 of the positive contribution of geostrophic advection, balanced by the weaker negative
740 contribution of horizontal and vertical Ekman advections. Note the weak spread of both the latter
741 ($\text{IQR} < 2 \text{ W m}^{-2}$). Finally, the individual residuals were obtained as the difference between the
742 tendency estimated from the mean CTDs, minus the adjusted net heat fluxes and total advection
743 from the various models. The residuals (last column of Figure 12a) are weak and poorly spread
744 (median = 1 W m^{-2} , $\text{IQR} = 3 \text{ W m}^{-2}$).

745 This means that the heat budget, estimated from various datasets and model outputs, can be
746 considered almost closed with the adjusted fluxes. This is not the case with the NWPM fluxes,
747 for which the heat budget is far from closure. The median of the residuals obtained with the
748 NWPM fluxes (calculated with the tendency deduced from CTDs and with the MERCATOR
749 geostrophic advection) was estimated to $+18 \text{ W m}^{-2}$, i.e., nearly the same order of magnitude as
750 the geostrophic advection term. Actually, NWPM provide surface fluxes computed without any
751 oceanic constraint, apart from the SSTs used in bulk parameterization. On the contrary, the
752 inverse method applied in the present study, is highly constrained by the realistic simulation of
753 the underlying whole water column and in particular by the observed heat and water budgets
754 through the minimization of the cost function.

755 Note that in our best flux estimates (represented by the red dots in Figure 12a), the negative
756 tendency term results from the balance between the dominant negative surface flux term and the
757 positive geostrophic advection term, plus the both slightly negative horizontal and vertical
758 Ekman advection terms. This result means that during the period considered, advection, mostly
759 its geostrophic component, was actively bringing heat from the surroundings toward the
760 convective area in compensation of the surface heat loss. In addition, Figure 12a shows that
761 errors on the adjusted fluxes can be mainly attributed to errors on geostrophic advection of
762 temperature, an important term in the first top 150 meters (see Figure 6).

763 The same budget was estimated for salinity (Figure 12b). The different terms (multiplied by $\rho_0 C_p$
764 times the saline contraction coefficient and divided by the thermal expansion coefficient) were
765 rescaled into $W m^{-2}$ to be compared with the heat budget. The median of the tendency term is
766 closed to zero, meaning that between MOOSE 2012 and MOOSE 2013, the various estimates led
767 to a quasi-balance between positive surface fluxes and negative advection. Positive surface
768 fluxes correspond to an excess of evaporation over precipitation rates over the test area. Figure
769 12b also allows to conclude that the water budget is more difficult to close than for heat (the
770 median of the residual is $+5 W m^{-2}$ compared with $+1 W m^{-2}$ for heat). This is mainly due to the
771 spread of geostrophic advection (IQR = $11 W m^{-2}$), larger than the spread of geostrophic
772 advection for heat (IQR = $8 W m^{-2}$). This illustrates the importance of salt injection into the
773 area. As mentioned in the previous subsection, all the NWPM water fluxes overestimate the
774 adjusted E-P fluxes, and all the residuals of the water budgets estimated with the NWPM are
775 higher (median = $+7 W m^{-2}$) than the ones obtained with the adjusted fluxes.

776 5. Conclusions

777 Two sets of surface fluxes were produced, the first one on an area of 300 km x 300 km in the
778 north-western Mediterranean (NWM), the second on a wider area (1000 km x 700 km). The first
779 dataset, the guess, was obtained from the best available products collected from several
780 platforms (satellites and model outputs) to calculate each component of the surface heat and
781 water fluxes on a 0.02° longitude x 0.02° latitude grid. These fluxes, spatially averaged, were
782 used to force a single-column model (SCM) and to simulate the evolution of mean potential
783 temperature and salinity profiles for this region. Through the specific form of its equations, the
784 model was also able to represent the evolution of subgrid scales. The SCM was forced by
785 advection terms: horizontal and vertical Ekman advectons deduced from the guess fields, and
786 geostrophic advection deduced from a 3D model, which, by assimilating altimetry, represented
787 realistically the large-scale oceanic circulation of the NWM.

788 After running some 50,000 SCM simulations, chosen by a genetic algorithm in varying 7
789 adjustable parameters –two model parameters and five coefficients correcting the surface
790 fluxes—, a best simulation was obtained. Using the optimized set of adjustable parameters, the
791 hourly surface flux guess was corrected at each point of the grid on which they were initially
792 calculated (as well as on a larger domain): this is the second surface flux dataset, or adjusted

793 fluxes. This dataset was thus directly derived from the closure of the heat and water budgets
794 which were observed in the region. Indeed, with the optimization by the genetic algorithm, the
795 model trajectory was forced to be close to the observations used in the cost function. This means
796 that in the inverse method, the fluxes were highly constrained by the underlying ocean layers,
797 and not only by SSTs, as was the case with the flux guess. More generally, in NWPM, in satellite
798 retrievals and in fluxes merged from model outputs and from satellite retrievals, SSTs are the
799 only weak oceanic constraints acting on the surface fluxes. Accordingly, the examples provided
800 in section 4, which compare the ARPEGE, AROME, NCEP, ECMWF and ERA-INTERIM
801 models, not only display a large spread but also a poor capacity to close the heat and water
802 budgets of the NWM.

803 The ultimate goal of surface fluxes is to force three-dimensional ocean models and to simulate
804 realistically the surface layers without any flux correction or relaxation, to obtain a correct
805 description of surface, mid-depth and deep water masses, and to produce an oceanic circulation
806 in agreement with the water masses produced. The same inverse method has already been
807 applied successfully in a low-energetic region of the northeast Atlantic [*Caniaux et al.*, 2005b].
808 Here, we showed that the same inverse method could be applied with only minor adaptation in a
809 distinct, more energetic area, also characterized by intermittent wintertime deep convection. The
810 flux dataset produced, which takes into account the oceanic mesoscale, is thought to improve
811 simulations in this area of the Mediterranean Sea, more precisely the intensity and timing of
812 oceanic deep convective events, and to help reduce errors on surface fluxes, the major problem
813 of numerical simulations in this basin [e.g., *Tsimplis et al.*, 2006; *Béranger et al.*, 2010; *Jordà et*
814 *al.*, 2016].

815 **Acknowledgments**

816 This work is a contribution to the HyMeX program (HYdrological cycle in the Mediterranean
817 EXperiment - www.hymex.org) through INSU-MISTRALS support and through the ASICS-
818 MED project (Air-Sea Interaction and Coupling with Submesoscale structures in the
819 MEDiterranean, ANR-2012-BS06-003. [http://www.agence-nationale-
820 recherche.fr/?Project=ANR-12-BS06-0003](http://www.agence-nationale-recherche.fr/?Project=ANR-12-BS06-0003) and <http://www.hymex.org/asicsmed/>). The authors
821 acknowledge Mercator-Océan for supplying the PSY2V4R4 analyses and the HyMeX database
822 teams (ESPRI/IPSL and SEDOO/OMP) for their help in accessing the data. We are indebted to

823 Vincent Tallandier and Loïc Houpert for calibrating the data of the MOOSE campaigns and
824 mooring data, to Claude Estournel for supplying the SYMPHONY model outputs, Valérie
825 Garnier and Pierre Garreau those of MARS3D and Jonathan Beuvier those of MEDRYS. Special
826 thanks are dedicated to the National Climatic Data Center for making TRMM data available
827 online as well as the Centre de Météorologie Spatiale (Météo-France, Lannion) for the radiative
828 fluxes downloaded from <ftp://eftp.ifremer.fr/cersat-rt/project/osi-saf/data/radflux/13/msg2/hourly/>
829 and the SSTs downloaded from <ftp://eftp.ifremer.fr/cersat-rt/project/medspiration/data/14/med/odyssea/>. We also thank all the participants to the
830 hydrological surveys, their scientific leaders and crew members.
831
832

832 **References**

- 833
- 834 Alhammoud, B., C. Claud, B.M. Fanatsu, K. Béranger, and J.-P. Chaboureau (2014), Patterns of
835 precipitation and convection occurrence over the Mediterranean basin derived from a decade of
836 microwave satellite observations, *Atmosphere*, *5*, 370-398, doi:10.3390/atmos5020370.
- 837
- 838 Anderson, R.J. (1993), A study of wind stress and heat flux over the open ocean by the inertial-
839 dissipation method, *J. Phys. Oceanogr.*, *23*, 2153-2161.
- 840
- 841 Artale, V., D. Iudicone, R. Santoleri, V. Rupolo, S. Marullo, and F. D'Ortenzio (2002), Role of
842 surface fluxes in ocean general circulation models using satellite sea surface temperature:
843 Validation of and sensitivity to the forcing frequency of the Mediterranean thermohaline
844 circulation, *J. Geophys. Res.*, *107* (C8), doi:10.1029/2000JC000452.
- 845
- 846 Barnier, B., L. Siefridt, and P. Marchesiello (1995), Thermal forcing for a global ocean
847 circulation model using three-year climatology of ECMWF analyses, *J. Mar. Syst.*, *6*, 363-380.
- 848
- 849 Béranger, K., B. Barnier, S. Gulev, and M. Crépon (2006), Comparing 20 years of precipitation
850 estimates from different sources over the world ocean, *Ocean Dyn.*, *56*, 104-138.
- 851
- 852 Béranger, K., Y. Drillet, M.-N. Houssais, P. Testor, R. Bourdallé-Badie, B. Alhammoud, A.
853 Bozec, L. Mortier, P. Bouruet-Aubertot, and M. Crépon (2010), Impact of the spatial distribution
854 of the atmospheric forcing on water mass formation in the Mediterranean sea, *J. Geophys. Res.*,
855 *115*, C12041, doi:10.1029/2009JC005648.
- 856
- 857 Bignami, F., S. Marullo, R. Santoleri, and M.E. Schiano (1995), Longwave radiation budget in
858 the Mediterranean Sea, *J. Geophys. Res.*, *100*, 2501-2514.
- 859
- 860 Bourassa, M., S.T. Gille, C. Bitz, D. Carlson, I. Cerovecki, C.A. Clayson, M.F. Cronin, W.M.
861 Drennan, C.W. Fairall, R.N. Hoffman, G. Magnusdottir, R.T. Pinker, I.A. Renfrew, M. Serreze,
862 K. Speer, L.D. Talley, and G.A. Wick (2013), High latitude ocean and sea ice surface fluxes:

863 challenges for climate research, *Bull. Am. Meteor. Soc.*, 94(3), 403-423, doi: 10.1175/BAMS-D-
864 11-00244.1.

865

866 Bouttier, F. (2007), The forthcoming AROME regional forecasting system, *La Météorologie*, 58,
867 12-20, doi:10.4267/2042/18203.

868

869 Bowman, K.P., C.R. Homeyer, and D.G. Stone (2009), A comparison of oceanic precipitation
870 estimates in the tropics and subtropics, *J. Appli. Meteor. Climatol.*, 48, 1335-1344.

871

872 Brisson, A., P. Le Borgne, and A. Marsouin (1999), Surface solar irradiance retrieval from
873 GOES data in the framework of the Ocean and Sea Ice Application Facility, *Proceedings of the*
874 *1999 EUMETSAT Meteorological Satellite Data User's Conference*, Copenhagen, 6-10
875 September 1999.

876

877 Brisson, A., P. Le Borgne, and A. Marsouin (2001), OSI SAF radiative fluxes : pre-operational
878 results, *Proceedings of the 2001 EUMETSAT Meteorological Satellite Data User's Conference*,
879 Antalya, 1-5 October 2001.

880

881 Brut, A., A. Butet, P. Durand, G. Caniaux, and S. Planton (2005), Air-sea exchanges in the
882 equatorial area from the EQUALANT99 dataset: Bulk parameterizations of turbulent fluxes
883 corrected for airflow distortion, *Q. J. R. Meteorol. Soc.*, 131, 2497-2538,
884 doi:10.125/qj.03.185.

885

886 Caniaux, G., A. Brut, D. Bourras, H. Giordani, A. Paci, L. Prieur, and G. Reverdin (2005a), A
887 one year sea surface heat budget in the northeastern Atlantic basin during the POMME
888 experiment: 1. Flux estimates, *J. Geophys. Res.*, 110, C07S02, doi:10.1029/2004JC002596.

889

890 Caniaux, G., S. Belamari, H. Giordani, A. Paci, L. Prieur, and G. Reverdin (2005b), A one year
891 sea surface heat budget in the northeastern Atlantic basin during the POMME experiment: 2.
892 Flux optimization, *J. Geophys. Res.*, 110, C07S03, doi:10.1029/2004JC002695.

893

894 Caniaux, G., H. Giordani, L. Prieur, R. Waldman, J. Beuvier, C. Estournel, V. Garnier, and P.
895 Garreau (2015), Physical processes from a 1D column model simulation of the North-western
896 Mediterranean basin from August 2012 to August 2013, HyMeX 9th International Workshop,
897 Mykonos, Greece, 21-25 September 2015.

898

899 Carroll, D.L. (1996), Genetic algorithms and optimizing chemical oxygen-iodine lasers, in
900 *Developments in Theoretical and Applied Mechanics*, vol. XVIII, Edited by H.B. Wilson et al.,
901 pp. 411-424, Sch. of Eng. Univ. of Ala., Tuscaloosa.

902

903 Castellari, S., N. Pinardi, and K. Leaman (1998), A model study of air-sea interactions in the
904 Mediterranean Sea, *J. Mar. Syst.*, 18, 89-114, doi:10.1016/S0924-7963(98)90007-0.

905

906 Castellari, S., N. Pinardi, and K. Leaman (2000), Simulation of the water mass formation
907 processes in the Mediterranean Sea: influence of the time frequency of the atmospheric forcing,
908 *J. Geophys. Res.*, 105(C10), 24,157–24,181, doi: 10.1029/2000JC900055.

909

910 Conan, P. (2013), DeWEX-MerMex 2013 leg2 cruise, R/V Le Suroît, *Tech. Rep.*,
911 doi :10.17600/13020030.

912

913 Courtier, P., C. Freydier, J.-F. Geleyn, F. Rabier, and M. Rochas (1991), The ARPEGE project at
914 Météo-France, in *ECMWF 1991 Seminar Proceedings: Numerical Methods in Atmospheric*
915 *Models, ECMWF, 9-13 September 1991*, vol. 2, pp. 123-231, Eur. Cent. For Medium-Range
916 Weather Forecasts, Reading U.K.

917

918 Cronin, M.F., M. Bourassa, C.A. Clayson, J. Edson, C. Fairall, R.A. Feely, E. Harisson, S. Josey,
919 M. Kubota, B.P. Kumar, K. Kutsuwada, B. Large, J. Mathis, M. McPhaden, L. O'Neill, R.
920 Pinker, K. Takahashi, H. Tomita, R.A. Weller, L. Yu, and C. Zhang (2014), Wind stress and air-
921 sea fluxes observations : status, implementation and gaps, A white paper for the Tropical Pacific
922 Observing System of 2020 Workshop (TPOS-2020).

923

924 Curry, J.A., C.A. Clayson, W.B. Rossow, R. Reeder, Y.C. Zhang, P.J. Webster, G. Liu, and R.S.
925 Sheu (1999), High-resolution satellite-derived dataset of the surface fluxes of heat, freshwater
926 and momentum for the TOGA COARE IOP, *Bull. Am. Meteorol. Soc.*, *80*, 2059-2080.

927

928 Cushman-Roisin, B. (1987), *Dynamics of the oceanic surface mixed layer*, Edited by P. Muller
929 and D. Henderson, Hawaii Inst. of Geophys., Honolulu.

930

931 DeCosmo, J., K.B. Katsaros, S.D. Smith, R.J. Anderson, W.A. Osst, K. Bumke, and H.
932 Chadwick (1996), Air-sea exchange of sensible heat and water vapor: the HEXOS results, *J.*
933 *Geophys. Res.*, *101*, 12001-12016.

934

935 Dee, D.P., et al. (2011), The ERA-INTERIM reanalysis: configuration and performance of the
936 data assimilation system, *Q. J. R. Meteorol. Soc.*, *137*, 553-597, doi:10.1002/qj.828.

937

938 De Mey, P., and Y. Ménard (1989), Synoptic analysis and dynamical adjustment of GOES-3 and
939 SEASAT altimeter eddy fields in the north-west Atlantic, *J. Geophys. Res.*, *94*, 6221-6230.

940

941 Donlon, C. J., M. Martin, J. D. Stark, J. Roberts-Jones, E. Fiedler, and W. Wimmer (2012), The
942 Operational Sea Surface Temperature and Sea Ice analysis (OSTIA), *Remote Sensing of*
943 *Environment*, *116*, 140-158, doi: 10.1016/j.rse.2010.10.017 2011.

944

945 Drillet, Y., J.-M. Lellouche, B. Levier, M. Drevillon, O. Le Galloudec, G. Reffray, C. Regnier,
946 E. Greiner, and M. Clavier (2014), Forecasting the mixed-layer depth in the Northeast Atlantic:
947 an ensemble approach, with uncertainties based on data from operational forecasting systems,
948 *Ocean Sci.*, *10*, 1013-1029, doi:10.5194/os-10-1013-2014.

949

950 Drobinski, P., et al. (2014), HymeX, a 10-year multidisciplinary program on the Mediterranean
951 water cycle, *Bull. Am. Meteorol. Soc.*, *95*, 1063-1082, doi :10.1175/BAMS-D-12-00242.1.

952

953 Ducrocq, V., et al. (2014), HyMeX-SOP1, the field campaign dedicated to heavy precipitation
954 and flash flooding in the Northwestern Mediterranean, *Bull. Am. Meteorol. Soc.*, *95*, 1083-1100,
955 doi :10.1175/BAMS-D-12-00244.1.

956

957 Dupuis, H., C. Guérin, D. Hauser, A. Weill, P. Nacass, W. Drennan, S. Cloché, and H. Graber
958 (2003), Impact of flow distortion corrections on turbulent fluxes estimated by the inertial
959 dissipation method during the FETCH experiment on R/V L'Atalante, *J. Geophys. Res.*,
960 *108*(C3), 8064, doi:10.1029/2001JC001075.

961

962 Durrieu de Madron, X., et al. (2013), Interaction of dense shelf water cascading and open-sea
963 convection in the northwestern Mediterranean during winter 2012, *Geophys. Res. Lett.*, *40*, 1379-
964 1385, doi:10.1002/grl.50331.

965

966 Estournel, C., et al. (2016a), HymeX-SOP2, the field campaign dedicated to dense water
967 formation in the Northwestern Mediterranean, *Oceanogr.*, in revision.

968

969 Estournel, C., P. Testor, P. Damien, F. D'Ortenzio, P. Marsaleix, P. Conan, F. Kessouri, X.
970 Durrieu de Madron, L. Coppola, J.-M. Lellouche, S. Belamari, L. Mortier, C. Ulses, M.-N.
971 Bouin, and L. Prieur (2016b), High resolution modeling of dense water formation in the north-
972 western Mediterranean during winter 2012-2013: processes and budget, *J. Geophys. Res.*,
973 doi:10.1002/2016JC011935.

974

975 Eymard, L., G. Caniaux, H. Dupuis, L. Prieur, H. Giordani, R. Troadec, P. Bessemoulin, G.
976 Lachaud, G. Bouhours, D. Bourras, C. Guérin, P. Le Borgne, A. Brisson, and A. Marsouin
977 (1999), Surface fluxes in the North Atlantic current during CATCH/FASTEX, *Q. J. R. Meteorol.*
978 *Soc.*, *125*(561), 3563-3599.

979

980 Fairall, C.W., E.F. Bradley, J.E. Hare, A.A. Grachev, and J.B. Edson (2003), Bulk
981 parameterization of air-sea fluxes: updates and verification for the COARE algorithm, *J. Clim.*,
982 *16*(4), 571-591.

983

- 984 Garreau, P., V. Garnier, and A. Schaeffer (2011), Eddy resolving modelling of the Gulf of Lions
985 and Catalan Sea, *Ocean Dyn.*, *61*, 991–1003, doi:10.1007/s10236-011-0399-2.
986
- 987 Gascard, J.C. (1978), Mediterranean deep water formation, baroclinic instability and oceanic
988 eddies, *Oceanologica Acta*, *1*, 315-330.
989
- 990 Gaspar, P., Y. Grégoris, and J.-M. Lefèvre (1990a), A simple eddy kinetic energy model for
991 simulations of the oceanic vertical mixing: test a station PAPA and long-term upper ocean study
992 site, *J. Geophys. Res.*, *95*, 16,179-16,193.
993
- 994 Gaspar, P., J.-C. André, and J.-M. Lefèvre (1990b), The determination of latent and sensible heat
995 fluxes at the ocean-atmosphere interface viewed as an inverse problem, *J. Geophys. Res.*, *95*,
996 16,169-16,178.
997
- 998 Giordani, H., G. Caniaux, L. Prieur, A. Paci, and S. Giraud (2005), A one year mesoscale
999 simulation of the northeast Atlantic: mixed layer heat and mass budgets during the POMME
1000 experiment, *J. Geophys. Res.*, *110*, C07S08, doi:10.1029/2004JC002765.
1001
- 1002 Giordani, H., P. Testor, L. Coppola, L. Prieur, I. Taupier-Letage, M.-N. Bouin, G. Caniaux, C.
1003 Lebeaupin, M. Hermann, and F. D'Ortenzio (2014), A multiplatform fine scale 3D analysis of the
1004 Northwestern Mediterranean during the HyMeX/ASICS Experiment: application to dense water
1005 formation, HyMeX 8th International Workshop, Valletta (Malta), 15-18 September.
1006
- 1007 Grist, J.P., and S.A. Josey (2003), Inverse analysis adjustment of the SOC air-sea flux
1008 climatology using ocean heat transport constraints, *J. Clim.*, *16*, 3274-3295.
1009
- 1010 Hamon, M., J. Beuvier, S. Somot, J.-M. Lellouche, E. Greiner, G. Jordà, M.-N. Bouin, T.
1011 Arsouze, K. Béranger, F. Sevault, C. Dubois, M. Drevillon, and Y. Drillet (2016), Design and
1012 validation of MEDRYS, a Mediterranean Sea reanalysis over the period 1992-2013, *Ocean Sci.*,
1013 *12*, 577-599, doi:10.5194/os-12-577-2016.
1014

1015 Herrmann, M., and S. Somot (2008), Relevance of ERA40 dynamical downscaling for modeling
1016 deep convection in the Mediterranean Sea, *Geophys. Res. Lett.*, *35*, L04607,
1017 doi:10.1029/2007GL032442.

1018

1019 Herrmann, M., J. Bouffard, and K. Béranger (2009), Monitoring open-ocean deep convection
1020 from space, *Geophys. Res. Lett.*, *36*, L03606, doi:10.1092/2008GL036422.

1021

1022 Houpert, L., X. Durrieu de Madron, P. Testor, A. Bosse, F. D'Ortenzio, M.-N. Bouin, D. Dausse,
1023 H. Le Goff, S. Kunesch, M. Labaste, L. Coppola, L. Mortier, and P. Raimbault (2016),
1024 Observations of open-ocean deep convection in the Northwestern Mediterranean Sea: seasonal
1025 and interannual variability of mixing and deep water masses for the 2007-2013 period, *J.*
1026 *Geophys. Res.*, submitted.

1027

1028 Huffman, G.J., R.F. Adler, D.T. Bolvin, G. Gu, E.J. Nelkin, K.L. Bowman, E.F. Stocker, and
1029 D.B. Wolff (2007), The TRMM multi-satellite precipitation analysis: quasi-global, multi year,
1030 combined-sensor precipitation estimates at fine scale, *J. Hydrometeorol.*, *8*, 33-55.

1031

1032 Isemer, H.J., J. Willebrand, and L. Hasse (1989), Fine adjustment of large scale air-sea energy
1033 flux parameterizations by direct estimates of ocean heat transport, *J. Clim.*, *2*, 1173-1184.

1034

1035 Jerlov, N.G. (1976), *Marine Optics, Elsevier Oceanogr. Ser.*, vol. 14, 231pp., Elsevier, New
1036 York.

1037

1038 Jordà, G., K. von Schuckmann, S.A. Josey, G. Caniaux, J. García-Lafuente, S. Sammartino, E.
1039 Özsoy, J. Polcher, G. Notarstefano, P.-M. Poulin, F. Adloff, J. Salat, C. Naranjo, K. Schroeder, J.
1040 Chiggiato, G. Sannino, and D. Macías (2016), The Mediterranean Sea heat and mass budgets:
1041 estimates, uncertainties and perspectives, *Prog. Oceanogr.*, submitted.

1042

1043 Kantha, L.H., and C.A. Clayson (1994), An improved mixed layer model for geophysical
1044 applications, *J. Geophys. Res.*, *99*, 25,235-25,266.

1045

- 1046 Killworth, P.D., D. Smeed, and A. Nurser (2000), The effects on ocean models of relaxation
1047 toward observations at the surface, *J. Phys. Oceanogr.*, *30*, 160-174.
1048
- 1049 Large, W.G., J.C. McWilliams, and S. Doney (1994), Ocean vertical mixing: a review and a
1050 model with a nonlocal boundary layer parameterization, *Rev. Geophys.*, *32*, 363-403.
1051
- 1052 Large, W.G., and S.G. Yeager (2009), The global climatology of an interannually varying air-
1053 sea flux data set, *Clim. Dyn.*, *33*(2-3), 341-364.
1054
- 1055 Leaman, K. D., and F. Schott (1991), Hydrographic structure of the convection regime in the
1056 Golfe du Lion, *J. Phys. Oceanogr.*, *21*, 575-598.
1057
- 1058 Le Borgne, P., G. Legendre, and A. Marsouin (2007), Validation of the OSISAF radiative fluxes
1059 over the equatorial Atlantic during AMMA experiment, Proceedings of the Joint 2007
1060 EUMETSAT and American Meteorological Society Conference, Amsterdam, The Netherlands,
1061 24-28 September 2007, ISBN 92-9110-076-5, ISSN 1011-3932.
1062
- 1063 Liu, C., R.P. Allan, P. Berrisford, M. Mayer, P. Hyder, N. Loeb, D. Smith, P.-L. Vidale, and J.M.
1064 Edwards (2015), Combining satellite observations and reanalysis energy transports to estimate
1065 global net surface energy fluxes 1985-2012, *J. Geophys. Res. Atmos.*, *120*(18), 9374-9389,
1066 doi:10.1002/2015JD023264.
1067
- 1068 MacDonald, A.M., and C. Wunsch (1996), An estimate of global ocean circulation and heat
1069 fluxes, *Nature*, *382*, 436-439.
1070
- 1071 Madec, G., F. Lott, P. Delecluse, and M. Crépon (1996), Large-scale preconditioning of deep-
1072 water formation in the northwestern Mediterranean Sea, *J. Phys. Oceanogr.*, *26*, 1393-1408,
1073 doi:10.1175/1520-0485(1996)026<1393:LSPODW>2.0CO ;2.
1074

- 1075 Marsaleix, P., F. Auclair, and C. Estournel (2009), Low-order pressure gradient schemes in
1076 sigma coordinate models: the seamount test revisited, *Ocean Modell.*, *30*, 169-177,
1077 doi:10.1016/j.ocemod.2009.06.011.
1078
- 1079 Marsaleix, P., F. Auclair, C. Estournel, C. Nguyen, and C. Ulses (2012), Alternatives to the
1080 Robert-Asselin filter, *Ocean Modell.*, *41*, 53-66, doi :10.1016/j.ocemod.2011.11.002.
1081
- 1082 Marshall, J., and F. Schott (1999), Open-ocean convection: observations, theory, and models,
1083 *Rev. Geophys.*, *37*(1), 1-64.
1084
- 1085 McDougall, T.J. (1987), Neutral surfaces, *J. Phys. Oceanogr.*, *17*(11), 1950-1964.
1086
- 1087 Mémery, L., G. Reverdin, J. Paillet, and A. Oschlies (2005), Introduction to the POMME special
1088 section: thermocline ventilation and biogeochemical tracer distribution in the northeast Atlantic
1089 Ocean and impact of mesoscale dynamics, *J. Geophys. Res.*, *110*, C07S01, 1-17,
1090 doi:10.1029/2005JC002976.
1091
- 1092 Millot, C. (1987), Circulation in the Western Mediterranean Sea, *Oceanol. Acta*, *10*(2), 143-149.
1093
- 1094 Paci, A., G. Caniaux, M. Gavart, H. Giordani, M. Lévy, L. Prieur, and G. Reverdin (2005), A
1095 high-resolution simulation of the ocean during the POMME experiment: simulation results and
1096 comparison with observations, *J. Geophys. Res.*, *110*, C07S09, doi:10.1029/2004JC002712.
1097
- 1098 Paci, A., G. Caniaux, H. Giordani, M. Lévy, L. Prieur, and G. Reverdin (2007), A high
1099 resolution simulation of the ocean during the POMME experiment: mesoscale variability and
1100 near surface processes, *J. Geophys. Res.*, *112*, C04007, doi:10.1029/2005JC003389.
1101
- 1102 Paulson, C.A., and J.J. Simpson (1977), Irradiance measurements in the upper ocean, *J. Phys.*
1103 *Oceanogr.*, *7*(6), 952-956.
1104

1105 Persson, P.O.G., J.E. Hare, C.W. Fairall, and W.D. Otto (2005), Air-sea interaction processes in
1106 warm and cold sectors of extratropical cyclonic storms observed during FASTEX, *Q. J. R.*
1107 *Meteorol. Soc.*, *131*, 877-912, doi:10.1256/qj.03.181.

1108

1109 Pettenuzzo, D., W.G. Large, and N. Pinardi (2010), On the corrections of ERA-40 surface flux
1110 products consistent with the Mediterranean heat and water budgets and the connection between
1111 basin surface total heat flux and NAO, *J. Geophys. Res.*, *115*, C06022,
1112 doi :10.1029/2009JC005631.

1113

1114 Pfeifroth, U., R. Mueller, and B. Ahrens (2013), Evaluation of satellite-based and reanalysis
1115 precipitation data in the tropical Pacific, *J. App. Met. and Clim.*, *52*, 634-644,
1116 doi:10.1175/JAMC-D-12-049.1.

1117

1118 Pickart, R.S., M.A. Spall, M.H. Ribergaard, G.W.K. Moore, and R.F. Milliff (2003), Deep
1119 convection in the Irminger Sea forced by the Greenland tip jet, *Nature*, *424*, 152-156,
1120 doi:10.1038/nature01729.

1121

1122 Poulain, P.M., M. Menna, and E. Mauri (2012), Surface geostrophic circulation of the
1123 Mediterranean Sea derived from drifter and satellite altimeter data, *J. Phys. Oceanogr.*, *42*(6),
1124 973-990, doi:10.1175/JPO-D-11-0159.1.

1125

1126 Rhein, M. (1995), Deep water formation in the western Mediterranean, *J. Geophys. Res.*, *100*,
1127 6943–6959, doi:10.1029/94JC03198.

1128

1129 Romanou, A., G. Tselioudis, C.S. Zerefos, C.A. Clayson, J.A. Curry, and A. Andersson (2010),
1130 Evaporation-precipitation variability over the Mediterranean and the Black Seas from satellite
1131 and reanalysis estimates, *J. Clim.*, *23*, 5268-5287, doi:10.1175/2010JCLI3525.1.

1132

1133 Roquet, H., S. Planton, and P. Gaspar (1993), Determination of ocean surface heat fluxes by a
1134 variational method, *J. Geophys. Res.*, *98*(C6), 10,211-10,221.

1135

- 1136 Rosati, A., and K. Miyakoda (1988), A general circulation model for upper ocean simulation, *J.*
1137 *Phys. Oceanogr.*, *18*, 1601-1626.
- 1138
- 1139 Ruti, P.M., S. Marullo, F. D'Ortenzio, and M. Tremant (2008), Comparison of analyzed and
1140 measured wind speeds in the perspective of oceanic simulations over the Mediterranean basin:
1141 Analyses, QuikSCAT and buoy data, *J. Mar. Syst.*, *70*, 33-48.
- 1142
- 1143 Sanchez-Gomez, E., S. Somot, S.A. Josey, C. Dubois, N. Elguindi, and M. Déqué (2011),
1144 Evaluation of Mediterranean Sea water and heat budgets simulated by an ensemble of high
1145 resolution regional climate models, *Clim. Dyn.*, *37*, 2067-2086, doi:10.1007/s00382-011-1012-6.
- 1146
- 1147 Send, U., J. Font, G. Krahnemann, C. Millot, M. Rhein, and J. Tintore (1999), Recent advances in
1148 observing the physical oceanography of the western Mediterranean Sea, *Prog. Oceanogr.*, *44*,
1149 37-64.
- 1150
- 1151 Serreze, M.C., A. Barrett, and F. Lo (2005), Northern high latitude precipitation as depicted by
1152 atmospheric reanalyses and satellite retrievals, *Mon. Weather Rev.*, *133*, 3407-3430.
- 1153
- 1154 Simmons, H.L., and I.V. Polyakov (2004), Restoring and flux adjustment in simulating
1155 variability of an idealized ocean, *Geophys. Res. Lett.*, *31*, L16201, doi:10.1029/2004GL020197.
- 1156
- 1157 Smith, S.D. (1980), Wind stress and heat flux over the ocean in gale force winds, *J. Phys.*
1158 *Oceanogr.*, *19*, 1208-1221.
- 1159
- 1160 Stammer, D., K. Ueyoshi, A. Köhl, W.G. Large, S.A. Josey, and C. Wunsch (2004), Estimating
1161 air-sea fluxes of heat, freshwater and momentum through global ocean data assimilation, *J.*
1162 *Geophys. Res.*, *109*, C05023, doi:10.1029/2003JC002082.
- 1163
- 1164 Testor, P., L. Coppola, and L. Mortier (2012), 2012 MOOSE-GE cruise, R/V Le Suroît, *Tech.*
1165 *Rep.*, doi:10.17600/12020030.
- 1166

- 1167 Testor, P., L. Coppola, and L. Mortier (2013a), 2013 MOOSE-GE cruise, R/V Le TethysII, *Tech.*
1168 *Rep.*, doi:10.17600/13450110.
- 1169
- 1170 Testor, P. (2013b), DeWEX-MerMex 2013 leg1 cruise, R/V Le Suroît, *Tech. Rep.*,
1171 doi:10.17600/13020010.
- 1172
- 1173 Trenberth, K.E. (1997), Using atmospheric budgets as a constraint on surface fluxes, *J. Clim.*,
1174 *10*, 2796-2809.
- 1175
- 1176 Tsimplis, M.N., V. Zverakis, S.A. Josey, E.L. Peneva, M.V. Struglia, E.V. Stanev, A.
1177 Theocharis, P. Lionello, P. Malanotte-Rizzoli, V. Artale, E. Tragou, and T. Oguz (2006), Chapter
1178 4 Changes in the oceanography of the Mediterranean sea and their link to climate variability, *in*
1179 *Developments in Earth and Environmental Sciences*, *4*, 227-282, doi:10.1016/S1571-
1180 9197(06)80007-8.
- 1181
- 1182 Valdivieso, M., K. Haines, M. Balmaseda, Y.-S. Chang, M. Drevillon, N. Ferry, Y. Fujii, A.
1183 Köhl, A. Storto, T. Toyoda, X. Wang, J. Waters, Y. Xue, Y. Yin, B. Barnier, F. Hernandez, A.
1184 Kumar, T. Lee, S. Masina, and K.A. Peterson (2015), An assessment of air-sea heat fluxes from
1185 ocean and coupled reanalyses, *Clim. Dyn.*, doi:10.1007/s00382-015-2843-3.
- 1186
- 1187 Wade, M., G. Caniaux, Y. DuPenhoat, M. Dengler, H. Giordani, and R. Hummels (2011), A one-
1188 dimensional modeling study of the diurnal cycle in the equatorial Atlantic at the PIRATA buoys
1189 during the EGEE-3 campaign, *Ocean Dyn.*, *61*(1), 1-20, doi:10.1007/s10236-010-0337-8.
- 1190
- 1191 Waldman, R., S. Somot, M. Herrmann, P. Testor, C. Estournel, F. Sevault, L. Prieur, L. Mortier,
1192 L. Coppola, V. Taillandier, P. Conan, and D. Dausse (2016), Estimating dense water volume and
1193 its evolution for the year 2012-2013 in the North-western Mediterranean Sea: an observing
1194 system simulation experiment approach, *J. Geophys. Res.*, submitted.
- 1195
- 1196 Yu, L., R.A. Weller, and B. Sun (2004), Improving latent and sensible heat flux estimates for the
1197 Atlantic Ocean (1988–1999) by a synthesis approach, *J. Clim.*, *17*, 373–393.

1198

1199 Yu, L., and R.A. Weller (2007), Objectively analyzed air-sea heat fluxes for the global ice-free
1200 oceans (1981-2005), *Bull. Am. Meteorol. Soc.*, 88, 527-539, doi:10.1175/BAMS-88-4-527.

1201

1202 Yuan, D., and M.M. Rienecker (2003), Inverse estimation of sea surface flux over the equatorial
1203 Pacific ocean: seasonal cycle, *J. Geophys. Res.*, 108(C8), 3247, doi:10.1029/2002JC001367.